공학박사학위논문

미세 사출 성형에서 다중공동금형 내부의 유동 양상 분석

Analysis of flow pattern inside multi-cavity system in micro injection molding

2019년 2월

서울대학교 대학원

기계항공공학부

김 범 래

공학박사학위논문

미세 사출 성형에서 다중공동금형 내부의 유동 양상 분석

Analysis of flow pattern inside multi-cavity system in micro injection molding

2019년 2월

서울대학교 대학원

기계항공공학부

김 범 래

Abstract

Analysis of flow pattern inside multi-cavity system in micro injection molding

Beom Rae Kim
Department of Mechanical and Aerospace Engineering
Seoul National University

Micro injection molding is manufacturing process widely used for thermoplasitcs because of its fast processing time and low cost. In micro-injection molding, there are two major defects which can be occurred in injection stage. One is the defect occurred by cavity filling deviation when the melted resin goes through the runner of mold, and the other is flow mark which is occurred in mold cavity. We investigated the relation between major defects and the major process conditions in micro-injection molding.

For finding the major process conditions which affect to the cavity filling deviation, we did numerical analysis. We investigated the relation between the cavity filling deviation and three process conditions (deviation of runner diameter, wall temperature and gate thickness) with two numerical results: filling fraction and filling time delay. We used the properties of EP-6000 in polypropylenes. Modified Cross model is used for simulating the rheological behavior of polymer. The result of CFD simulation showed that the major process conditions which affect to the cavity filling deviation were the deviation of runner diameter and wall temperature. The mixed condition of those two had the biggest cavity filling deviation.

For reducing cavity filling deviation, we suggested three robust designs: convergent runner model, reservoir model and complex model which is combined with those to models. all models reduced cavity filling deviation effectively, and the complex model had the biggest effect. The reduction of filling fraction was 33% in complex model.

For flow mark which is defect occurred in cavity, we did parametric study in according to “Go-Over” hypothesis. we found three major conditions which affects to the size of flow mark by this parametric study: injection speed, resin temperature and mold temperature. We investigated the relation between the size of flow mark and those three major process conditions by experiment and numerical analysis. The results of both analysis showed that the size of flow mark decreased when injection speed, resin temperature or mold temperature was increased. This result was exactly fitted with the result of parametric study. We also observed the contour of resin flow when the flow mark generated with CFD simulation and it was well fitted with "Go-Over" hypothesis.

Keywords: micro injection molding, multi-cavity system, cavity filling deviation, flow mark, numerical analysis, "Go-Over" hypothesis

Contents

Abstract i

Contents iv

List of tables vii

List of figures viii

Chapter 1 Introduction 2

- 1.1 Overview 2
- 1.2 Cavity filling deviation 4
- 1.3 Flow mark 6
  - 1.3.1 “Go-Over” hypothesis 7
- 1.4 Objectives of this study 9

Chapter 2 Numerical analysis on cavity filling deviation 13

- 2.1 Background theories 13
  - 2.1.1 Governing equations 13
  - 2.1.2 Solution algorithm of flow with moving free surfaces 16
  - 2.1.3 Pressure-velocity coupling scheme 19
  - 2.1.4 Material properties used in numerical analysis 19
- 2.2 Modeling and meshing 22

2.3 Boundary conditions 23

2.4 Numerical results 25

  2.4.1 Mold temperature variation 25

  2.4.2 Runner diameter variation 28

  2.4.3 Gate thickness variation 31

  2.4.4 Mixed condition 33

2.5 Robust designs for reducing cavity filling deviation 37

  2.5.1 Convergent runner model 38

    2.5.1.1 Head loss effect 38

    2.5.1.2 Results of convergent runner model 40

  2.5.2 Reservoir model 43

  2.5.3 Complex model 45

Chapter 3 Analysis on flow mark 49

3.1 Parametric study 49

3.2 Experimental analysis on flow mark 58

  3.2.1 Material for experiments 58

  3.2.2 Instrumentals for experiments 60

    3.2.2.1 Injection molding machine 60

    3.2.2.2 Mold specification 62

  3.2.3 Measurement of flow mark 63

3.2.4 Process conditions 65

3.2.5 Results of experimental analysis 66

3.3 Numerical analysis on flow mark 72

3.3.1 Validation of numerical analysis 73

3.3.2 Material properties used in numerical analysis 73

3.3.3 Modeling and meshing 78

3.3.4 Measurement of flow mark 79

3.3.5 Boundary conditions 79

3.3.6 Results of numerical analysis 81

3.3.6.1 Comparison with “Go-Over” hypothesis 81

3.3.6.2 Comparison with experimental results 82

Chapter 4 Conclusion 89

References 91

국문 초록 95

List of tables

Table 2.1 Values used in Cross-WLF model (EP-6000) 21

Table 2.2 Boundary conditions for complex case 25

Table 2.3 Numerical results of wall temperature case 26

Table 2.4 Numerical results of runner diameter case 28

Table 2.5 Numerical results of gate thickness case 31

Table 2.6 Numerical results of mixed condition 33

Table 2.7 Boundary conditions for results in figure 8 34

Table 2.8 Filling time delay and biggest filling fraction difference of each case 35

Table 2.9 Runner diameters of convergent runner model 41

Table 2.10 Numerical results of convergent runner model 42

Table 2.11 Numerical results of reservoir model 44

Table 2.12 Numerical results of complex model 46

Table 3.1 Thermophysical properties of LUPOY 60

Table 3.2 Specification of injection molding machine 61

Table 3.3 Process conditions for the flow mark experiments 65

Table 3.4 Values used in Cross-Arrhenius model (EP-7000) 77

Table 3.5 Boundary conditions for the flow mark simulations 80

List of figures

Figure 1.1	Schematic diagram of injection molding machine	2
Figure 1.2	Multi-cavity injection molding system	5
Figure 1.3	Flow marks on surface of sample	6
Figure 1.4	Flow mark generation process of “Go-Over” hypothesis illustrated schematically	8
Figure 2.1	Viscosity curves of polymer used in simulation using the Cross-WLF model	21
Figure 2.2	(a) Model and meshing for simulation (b) Intersection of first runners (c) End of second runner (d) Shape of gates	22
Figure 2.3	Boundary conditions for our simulation (a) Mold temperature case (reference temperature is 140°C) (b) Runner diameter case (reference diameter is 2.3 mm) (c) Gate thickness case (reference thickness is 0.3 mm) (d) mixed condition (reference mold temperature is 140°C and reference runner diameter is 2.3 mm)	24
Figure 2.4	Outlet mass flow rate of each runner in wall temperature case	27
Figure 2.5	Filling fraction and filling time delay of each runner in wall temperature case	27
Figure 2.6	Outlet mass flow rate of each runner in runner diameter case	30
Figure 2.7	Filling fraction and filling time delay of each runner in runner diameter case	30
Figure 2.8	Outlet mass flow rate of each runner in gate thickness case	32
Figure 2.9	Filling fraction and filling time delay of each runner in gate thickness case	32
Figure 2.10	Outlet mass flow rate of each runner in mixed condition	35

Figure 2.11	Filling fraction and filling time delay of each case	36
Figure 2.12	Geometry of robust designs **(a)** and **(b)** Convergent runner model **(c)** Reservoir model	37
Figure 2.13	(a) Basic concept of head loss (b) Head loss increase comparison between normal channel and convergent channel	39
Figure 2.14	The numbers of runners in convergent runner model	41
Figure 2.15	Outlet mass flow rate of each runner in convergent runner model	42
Figure 2.16	Outlet mass flow rate of each runner in reservoir model	44
Figure 2.17	Outlet mass flow rate of each runner in complex model	46
Figure 2.18	Filling fraction and filling time delay of each robust design model	47
Figure 3.1	Analysis model for generation of flow mark	51
Figure 3.2	Gauss error function	54
Figure 3.3	Relation between theta and two major process temperature (a) temperature of melted resin (b) temperature of mold wall	55
Figure 3.4	Volume-Temperature graph of used polymer (LUPOY)	59
Figure 3.5	Viscosity curves of used polymer (LUPOY)	59
Figure 3.6	Injection molding machine for experiments (SE50D, Sumimoto)	61
Figure 3.7	The shape of mold for the experiments	62
Figure 3.8	The sample made by the mold used for the experiments	63
Figure 3.9	Stylus 2D profiler (Alpha step P-500, KLA-Tencor)	64
Figure 3.10	3D surface of the sample	64
Figure 3.11	The depth of flow mark by changing injection speed (experimental result)	68

Figure 3.12	The width of flow mark by changing injection speed (experimental result)	68
Figure 3.13	The depth of flow mark by changing resin temperature (experimental result)	69
Figure 3.14	The width of flow mark by changing resin temperature (experimental result)	69
Figure 3.15	The depth of flow mark by changing mold temperature (experimental result)	70
Figure 3.16	The width of flow mark by changing mold temperature (experimental result)	70
Figure 3.17	The relation between the depth of flow marks and $\boldsymbol{\delta_{nf}/A}$ (experimental result)	71
Figure 3.18	The relation between the depth and the width of flow mark (experimental result)	71
Figure 3.19	The result of numerical analysis comparing to the result of experiment	72
Figure 3.20	Specific heat of the material used in simulation (EP-7000)	76
Figure 3.21	Thermal conductivity of the material used in simulation (EP-7000)	76
Figure 3.22	Viscosity curves of the material used in simulation using Cross-Arrhenius model (EP-7000)	77
Figure 3.23	Modeling of CFD simulation for flow mark generation	78
Figure 3.24	Meshing of the model used in CFD simulation for flow mark generation	78
Figure 3.25	The contour observation of flow mark generation	81
Figure 3.26	The depth of flow mark by changing injection speed (CFD simulation)	84
Figure 3.27	The width of flow mark by changing injection speed (CFD simulation)	84
Figure 3.28	The depth of flow mark by changing resin temperature (CFD simulation)	85

Figure 3.29 The width of flow mark by changing resin temperature (CFD simulation) 85

Figure 3.30 The depth of flow mark by changing mold temperature (CFD simulation) 86

Figure 3.31 The width of flow mark by changing mold temperature (CFD simulation) 86

Figure 3.32 The relation between the depth of flow marks and $\boldsymbol{\delta_{nf}/A}$ (CFD simulation) 87

Figure 3.33 The relation between the depth and the width of flow mark (CFD simulation) 87

Chapter 1

Introduction

1 Introduction

1.1 Overview

Micro-injection molding (MIM) is one of the key process for manufacturing thermoplastic microproducts or micro parts and is widely used as a cost effective replication method for mass production. [1] Recently, with the development of engineering plastics of good quality in their optical and physical properties, micro injection molding is becoming major process for manufacturing optical products such as micro lenses. A schematic diagram of typical injection molding machine is shown in Figure 1.1.

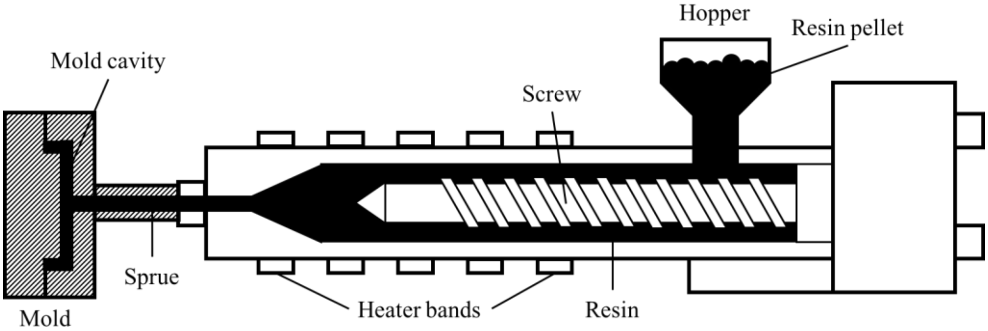

Figure 1.1 Schematic diagram of injection molding machine

MIM comprises largely of the following three steps[2]:

(a) the mold cavity equipped with a micro-structured tool (mold insert) is closed, evacuated, and heated above the glass transition temperature of the polymer.
(b) an injection unit heats the polymer and presses the viscous polymer into the mold.
(c) the polymer (and the tool) is cooled below its glass transition temperature and demolded from the tool.

Several surface defects may be obtained while the resin is being filled in the second step. Several of those defects are complimented by the high pressure in the packing stage after the second step, but some defects like unfilled cavity, weld lines, sink marks, and flow marks remain after the packing stage. [3]

In the injection stage, the melted polymer is injected into the sprue. Then it goes through the runner and fills the cavity for product consequently. The causes of defects in injection stage can be classified under two large groups.

The first is occurred when the melted polymer goes through the runner. Because of small scale of the product manufactured by micro-injection molding, multi-cavity system is widely used for increasing productivity. However, it is difficult to make the geometry of each runner in exactly same size because of the small size of the mold. Also, maintaining the temperature of each runner in same is difficult in actual process. because of these process problems, the deviation in the filling of each cavity can be occurred. This cavity filling deviation can be major cause for making defects in micro-injection molding.

The second is occurred when the melted polymer goes through the cavity. Because of the geometry of mold cavity or process conditions used, many defects can be occurred such as weld lines, blisters, burn marks, sink marks or flow marks. The flow mark is one of typical defects in injection molding process.

For a good replication of microparts, there are certain major process parameters: mold temperature, injection speed, injection pressure, holding time, holding pressure, etc. [4–7] These parameters are directly related to the factors that determine the quality of microproducts. Especially, surface quality is an important factor for micro-optical products. Therefore, it’s important to reveal the effects of major process conditions on surface quality of micro products, as the preceding research for reducing defects on micro products.

1.2 Cavity filling deviation

In classical macro scale injection molding, it is difficult to use multi-cavity mold because of mold size limitation. However, in micro injection molding, a cavity for micro product is so small compared to the mold, so multi cavity system can be used. Multi cavity system in micro injection molding has an advantage on mass production, but some new defects can arise with cavity filling deviation.

Recent studies are focused on establishing the cause of the surface defects or decreasing them by changing the parameters in experiments and visualizing unstable flow front using CFD simulations. However, in multi-cavity system, the balance regarding the filling of each cavity is also important. Flux goes into each cavity can have non-uniformity because of difference in temperature of each cavity, diameter of each runner or size of each cavity's gate. And this cavity filling deviation can affect productivity of injection molding.

Different studies investigate the relation between the parameters and cavity filling [8, 9], or the effect of mold geometry on cavity filling [10, 11], but there are not many studies focused on cavity filling deviation of multi-cavity systems. The representative multi-cavity system injection molding model is shown in Figure 1.2.

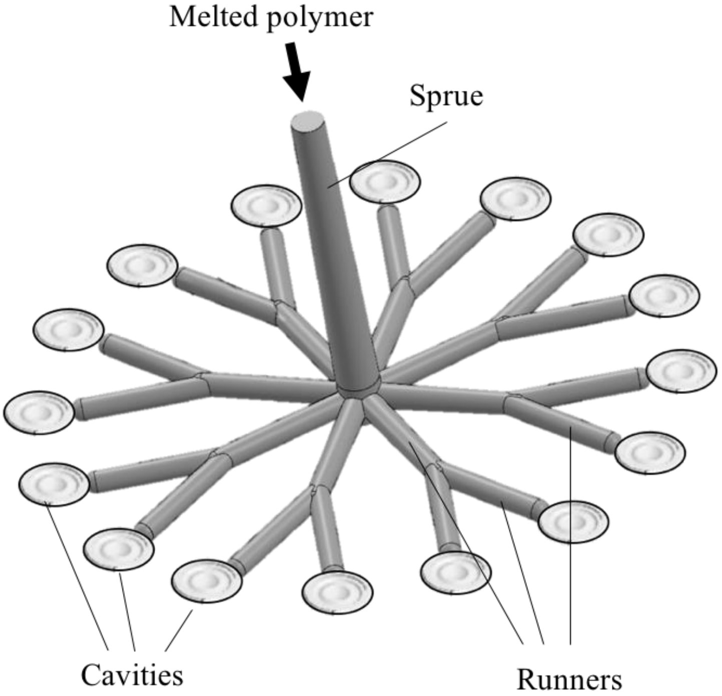

Figure 1.2 Multi-cavity injection molding system

1.3 Flow mark

When melted polymer is injected into the cavity during injection stage in injection molding, in certain conditions, wave-like surface with periodic hills and valleys oriented perpendicular to the main flow direction can arise. This phenomenon is known as flow mark. These wave-like flow mark phenomenon can appear in different type of polymers, including crystalline as well as amorphous polymer. [12-14] The typical shape of flow mark on surface of sample made by injection molding process is shown in Figure 1.3.

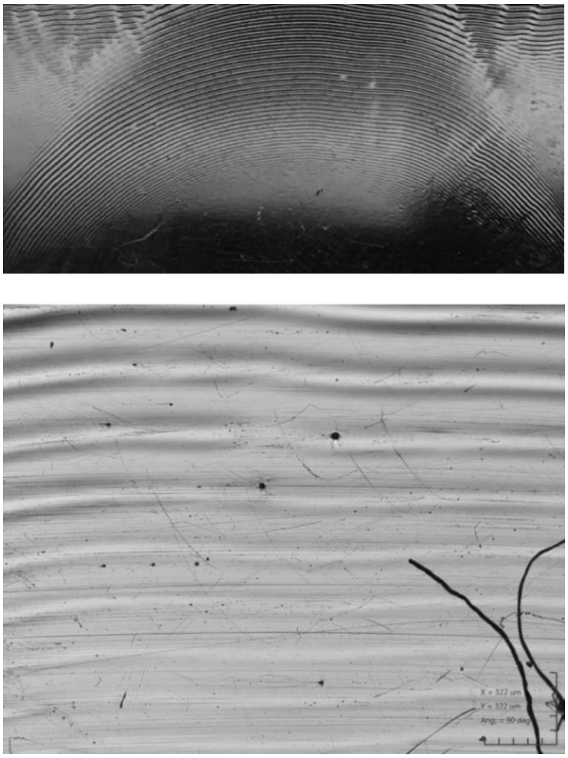

Figure 1.3 Flow marks on surface of sample

This phenomenon is commonly observed when the flow front velocity is relatively low (ranging from 1 to 200mm/s), and various processing conditions such as injection velocity, resin temperature, mold temperature and so on have effects on wavelength and depth of these flow marks.

The exact generation mechanism of this phenomenon is not revealed yet, however various hypotheses for this generation mechanism have been suggested such as "Go-Over hypothesis", "Buckling hypothesis", "Stick-Slip hypothesis" or "Thermal contraction hypothesis". [15]

1.3.1 "Go-Over" hypothesis

"Go-Over" hypothesis is one of the wave-like flow mark generation mechanism hypothesis. This hypothesis is first suggested by Yoshii et al. [12], and supported by Yokoi et al. [16] In injection stage of injection molding, molten polymer with high temperature is injected into the cavity mold with relatively low temperature, then the cooling takes place very rapidly. Because of this, a small portion of the flow front surface solidifies, and the still molten polymer above this solidified portion has to "Go-Over" this solidified melt, creating a gap. This gap takes places periodically, and consequently these gaps become wave-like flow marks.

The generation mechanism according to the "Go-Over" hypothesis could be summarized as follows. (Figure 1.4) During the filling stage of injection molding, molten polymer with high temperature touches the cold mold wall, and the surface nearest the walls solidifies first. Polymer melt is forced out to the flow front, spreads outward, and solidifies against the wall, while the solidified layer at contact line develops. The motion of the polymer melt is similar to that of water in a fountain (the effect is known as fountain flow). Due to the behavior of fountain flow, polymer melt above solidified layer goes over solidified region, forming periodic bright and dull bands, or wave-like flow marks. [12, 17]

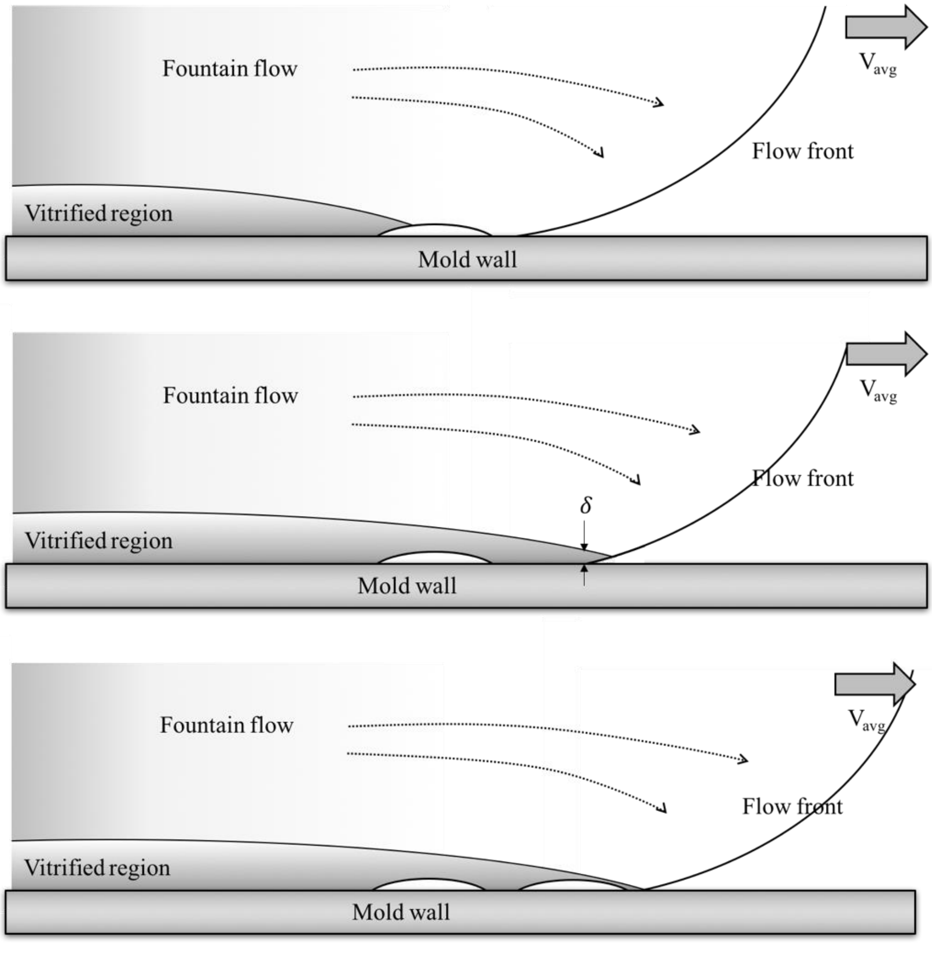

Figure 1.4 Flow mark generation process of “Go-Over” hypothesis illustrated schematically

In this study, we choose this “Go-Over” hypothesis as major flow mark generation mechanism. With this hypothesis, the wavelength and depth of flow mark have correlation, and these quantitative values of flow mark are affected by the process conditions such as the injection velocity, temperature difference between molten polymer and cavity mold, and viscosity change of molten polymer near the interface between molten polymer and mold wall. Therefore, we studied the effect of those conditions on the average size of flow mark.

1.4 Objectives of this study

These surface defects occurred in the surface of sample made by injection molding can be decreased or removed by high pressure in packing stage of injection molding process. But in optical products, one of most important products of micro-injection molding process, not only the surface defects which can be observed by naked eye but also the small defects like non-uniformity of density near the surface occurred by the defects before removed can be important factor of performance. In case of cavity filling deviation in multi-cavity micro injection process, the filling deviation can be also decreased in packing stage. But in case of the cavity filled earlier, the resin filled the cavity can be solidified earlier than other cavities and the pressure in packing stage cannot be fully transmitted to that cavity because of this solidification. Eventually, the packing pressure deviation can be occurred in each cavity and there can still be some surface defects left. Therefore, it is important to find the process conditions which can affect to the cavity filling deviation and to find the method to reduce it.

Flow marks can be also decreased in packing stage. But in our experiments and the earlier studies [12-15], they still existed in wave-like shape in surface of products or had density deviation pattern along the peak or valley of wave-like flow mark in injection stage. These defects after the packing stage can be important in some cases like optical products. Therefore, it is still important to find the relation between process conditions and the formation of flow marks in injection stage of micro injection molding process.

In this study, we focused on two major objectives. The first objective is focused on observing the major process condition that causes flux non-uniformity in multi-cavity micro-injection molding system by CFD simulations and suggesting the flow network for complementing the cavity filling deviation. We refer to this flow network as robust design. Considering the actual process, I constructed 16-cavity micro-injection mold and investigated the relation between the cavity filling deviation and three parameters: wall temperature, runner diameter, and gate size. Moreover, based on these results, we propose three robust designs: convergent model, reservoir model, and complex model (combination of the convergent and reservoir models), and observed the effect of these models on reducing the cavity filling deviation.

the second objective is observing the effects of major process conditions on average size of wave-like flow mark. We did parametric study in accordance with “Go-Over” hypothesis and investigated the relationship between flow mark size and the major process conditions through the result of parametric study. Both experimental analysis and numerical analysis were done, and we compared those results.

Chapter 2

Numerical analysis on cavity filling deviation

2 Numerical analysis on cavity filling deviation

As mentioned earlier, micro injection molding process with multi cavity system has significant advantages in productivity for mass production. Therefore, the overall trend for manufacturing micro products is using multi cavity system. In this multi cavity system, it is important to match the amount of flux into each cavity for making all micro products from cavities same. However, it is difficult to make the mold for multi cavity system perfectly match with blueprint in micro scale. Furthermore, it is nearly impossible to maintain a constant temperature for entire mold surface in general injection molding machine. With these difficulties, it is apt to have filling deviation between each cavity in multi cavity system. In this study, we focus on what process condition is major for making cavity filling deviation and suggest robust designs for reducing cavity filling deviation.

2.1 Background theories

2.1.1 Governing equations

The motion of polymer resin is governed by the conservation of mass and momentum. These conservation equations can be written for laminar flow as

$$\frac{\partial \rho}{\partial t} + \frac{\partial(\rho u)}{\partial x} + \frac{\partial(\rho v)}{\partial y} + \frac{\partial(\rho w)}{\partial z} = \mathrm{S}_m \tag{2.1}$$

$$\frac{\partial}{\partial t}(\rho \bar{v}) + \nabla \cdot (\rho \bar{v} \bar{v}) = -\nabla p + \nabla \cdot (\bar{\bar{\tau}}) + \rho \bar{g} + \bar{F} \tag{2.2}$$

Equation 2.1 is the general form of the mass conservation equation and is valid for incompressible as well as compressible flow. ρ is the density, u, v, and w are the velocity components in the x, y, and z directions, respectively, and S_m is the mass added to the continuous phase from the dispersed second phase (for example, due to vaporization of liquid droplets). In this study, we did not consider phase changes, thus, we assumed that $S_m = 0$. And the material is assumed to be incompressible during the filling stage for convenience. This assumption means that the density of the polymer resin is constant, so the first term of the equation 2.1 is neglected.

Equation 2.2 is the momentum conservation equation where p is the static pressure, $\bar{\tau}$ is the stress tensor, and $\rho \bar{g}$ and $\bar{F}$ are the gravitational body force and external body forces (for example, the ones that arise occur from interaction with the dispersed phase), respectively. As the phase change and the gravity force are neglected, $\bar{F} = 0$. The stress tensor $\bar{\tau}$ is given by

$$\bar{\tau} = \mu \left[\left(\nabla \bar{v} + \nabla \bar{v}^T - \frac{2}{3} \nabla \cdot \bar{v} I \right) \right] \tag{2.3}$$

where μ is the viscosity, I is the unit tensor, and the second term on the right hand side is the effect of volume dilation.

To include heat transfer in our simulation, an additional equation for energy conservation is solved.

$$\begin{aligned} &\frac{\partial}{\partial t}(\rho E) + \nabla \cdot \left(\bar{v}(\rho E + \rho)\right) \\ &= \nabla \cdot \left(k_{eff} \nabla T - \sum_{j} h_j \vec{J}_j + \left(\bar{\bar{\tau}}_{eff} \cdot \vec{v}\right) \right) \end{aligned} \tag{2.4}$$

where K_{eff} is the effective thermal conductivity and $\vec{J}_j$ is the diffusion flux of species j. The first three terms on the right-hand side represent the energy transfer due to conduction, species diffusion, and viscous dissipation, respectively. And E and h are given by ,

$$E = h - \frac{p}{\rho} + \frac{v^2}{2} \tag{2.5}$$

$$h = \sum_{j} Y_j h_j + \frac{p}{\rho} \tag{2.6}$$

In Equation (2.5), Y_j is the mass fraction of species j and

$$h_j = \int_{T_{ref}}^{T} C_{p,j} dT \tag{2.7}$$

The value used for T_{ref} is 298.15 K.

2.1.2 Solution algorithms of flow with moving free surfaces

For solving flows with moving free surfaces, we used Volume of Fluid (VOF) method. VOF method was first developed by Hirt and Nichols [18] and is one of representative algorithm based on a fixed coordinate system.

The volume of fluid $f(x, y, z, t)$ is defined as the volume fraction of fluid in an element, which can be expressed as

$$f = \frac{volume\ \ of\ \ fluid}{volume\ \ of\ \ element} \tag{2.8}$$

If $f = 1$, it means an element is fully filled with fluid and this element is considered as the main flow region. If $f = 0$, an element is empty and this empty element is excluded from the calculation of flow filed. If f lies between 0 and 1(i.e., $0 < f < 1$), the element is considered to be on the free surface and the calculation of field with free surface can be represented by using this variable f. The movement of flow front is represented by the following transport equation of f:

$$\frac{\partial f}{\partial t} + \mathbf{u} \cdot \nabla f = 0 \tag{2.9}$$

which states that the free surface is a material line. This equation for the movement of flow front represents only advection, so the solution by directly discretization can cause the smearing of flow front, called numerical diffusion. The effect of this numerical diffusion in the case of one-dimensional case is studied by Swaminathan and Voller. [19] VOF method is generally known for handling the flow with complex motion but it is problem that how to avoid this artificial diffusion and calculate advection without the smearing of flow front.

There are many researches for developing VOF method to reconstruct the shape of flow front and advance the free surface with the reconstructed geometry of interface. They contribute to increase the accuracy of numerical simulation result and to suppress the numerical diffusion. In 1976, Noh and Woodward [20] suggested Simple Line Interface Calculation (SLIC) method. In this method, the update of free surface is decomposed into x- and y-direction. All the surfaces are considered to be vertical for flux calculations in the x-direction and horizontal for flux calculation in the y-direction. Young [21] proposed that the line segment has a slope determined by considering the fractional volume of neighboring cells. In Hirt and Nichols' study [18], the free surface is reconstructed either horizontally or vertically in each surface cell, depending on its relation to neighboring cells. Also, they proposed donor-acceptor method. Those methods neglected the discontinuity of free surface at the boundary of elements for reconstructing the free surface and compressing the smearing of flow front.

However, Ashgriz and Poo [22] suggested Flux Line-segment model for Advection and Interface Reconstruction (FLAIR) method. In this method, the surface is approximated by a set of line segments fitted at the boundary of every two neighboring cells and the constructed interfaces become the continuous line segments. Recently, Piecewise-Linear Interface Calculation (PLIC) method is widely used for VOF method. In this method, the interface is assumed as a line or a plane whose normal vector is the gradient of f. [23] In our study, we also accept this VOF with PLIC method.

For tracking the free surface in a fixed grid system of VOF method, the volume flux calculation on every cell boundary is needed to be accurate. However, in VOF method, the fractional volume-of-fluid f is defined by elements, not by nodes. It means the different method is required for integrating the transport equation for the fractional volume-of-fluid f. Therefore, finite elements are used as cells or control volumes. The transport equation for the fractional volume-of-fluid in a conservative form is integrated over a cell.

$$\int_V \left[\frac{\partial f}{\partial t} + \mathbf{u} \cdot \nabla f\right] dV = 0 \tag{2.10}$$

combined this equation with divergence theorem, the results is as follows

$$\frac{\partial f}{\partial t} V_i + \int_\Gamma (\mathbf{u} \cdot \mathbf{n}) f d\Gamma = 0 \tag{2.11}$$

where Γ denotes the boundary of the domain and V_i is the volume of control volume.

2.1.3 Pressure-velocity coupling scheme

For pressure-velocity coupling scheme, we used the Pressure-Implicit with Splitting of Operators (PISO) algorithm. This PISO algorithm is part of the SIMPLE family of algorithm. It is based on the higher degree of the approximate relation between the corrections for pressure and velocity. [24] One of the limitations of the SIMPLE and SIMPLEC algorithms is that new velocities and corresponding fluxes don't satisfy the momentum balance after the pressure-correction equation is solved. With this limitation, the calculation should be repeated for satisfying the balance. The PISO algorithm performs neighbor correction and skewness correction for improving the efficiency of this calculation.

2.1.4 Material properties used in numerical analysis

The widely accepted Cross-WLF model is adopted with regard to the viscosity of the polymer material. The non-Newtonian behavior of the molten polymer can be characterized using this model. The model is given by

$$\eta(T,\dot{\gamma},P) = \frac{\eta_0(T,P)}{\left[1 + \frac{\eta_0(T)\cdot\dot{\gamma}}{\tau^*}\right]^{1-n}} \tag{2.12}$$

$$\eta_0(T,P) = D_1 exp\left(-\frac{C_1(T-T_0)}{C_2+T-T_0}\right) \tag{2.13}$$

$$T_0 = D_2 + D_3 \cdot P \tag{2.14}$$

where η_0 is zero-shear-rate viscosity, T is temperature, T_0 is glass transition temperature, P is pressure, τ^* is the critical stress level at the transition to shear thinning, $\dot{\gamma}$ is share rate, and n is power-law index in the high shear regime. The Cross-WLF model constants for the viscosity of the polymer material are shown in Table 2.1.

For the numerical analysis, we used the thermal characteristic values of EP-6000, the polymer resin in the polypropylene series. The polymer material is assumed to be incompressible. So, the density of the polymer material is constant in the entire simulation process, and its value is given as, ρ = 761.45 kg/m^3. The specific heat of melted polymer, C_p is $2870 J/kg \cdot K$, and the thermal conductivity k is $0.14\, W/m \cdot K$. We assumed that the properties of air and mold are constants.

Figure 2.1 shows the Cross-Arrhenius model with respect to values in Table 2.1. It indicates the viscosity of the polymer material used in this study based on the temperature and shear rate.

As mentioned before, the property values of the mold material and air are assumed to be constants for convenience of calculation. The density, specific heat, and thermal conductivity of the mold material are 8030 kg/m^3, 502.48 J/kg·K, and 16.27 W/m·K, respectively. Air is considered as an ideal gas, and the density, the specific heat, the thermal conductivity, and the viscosity of air are 1.225 kg/m^3, 1006.43 J/kg·K, 0.0242 W/m·K, and 1.7894×10^{-5} kg/m·s, respectively.

Table 2.1 Values used in Cross-WLF model (EP-6000)

Symbol	Value	Unit
n	0.3262	-
τ^*	16400	Pa
D_1	8.04e+11	Pa-s
D_2	263.15	K
D_3	0	K/Pa
C_1	24.75	K
C_2	51.6	K

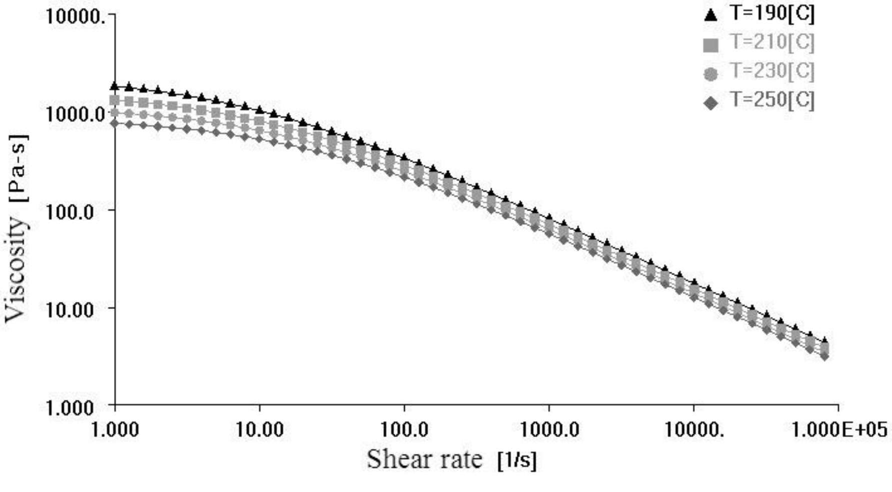

Figure 2.1 Viscosity curves of polymer used in simulation using the Cross-WLF model

2.2 Modeling and meshing

To observe the primary cause of cavity filling deviation, we considered a multi-cavity micro injection mold. Figure 2.2(a) shows the model that we used for our simulation. As can be seen, there is one sprue, intersection of first runners, 8 first runners, and 16 second runners. For each component, different meshing skills were used. The resin is injected into the top of the sprue, and it flows through the first and

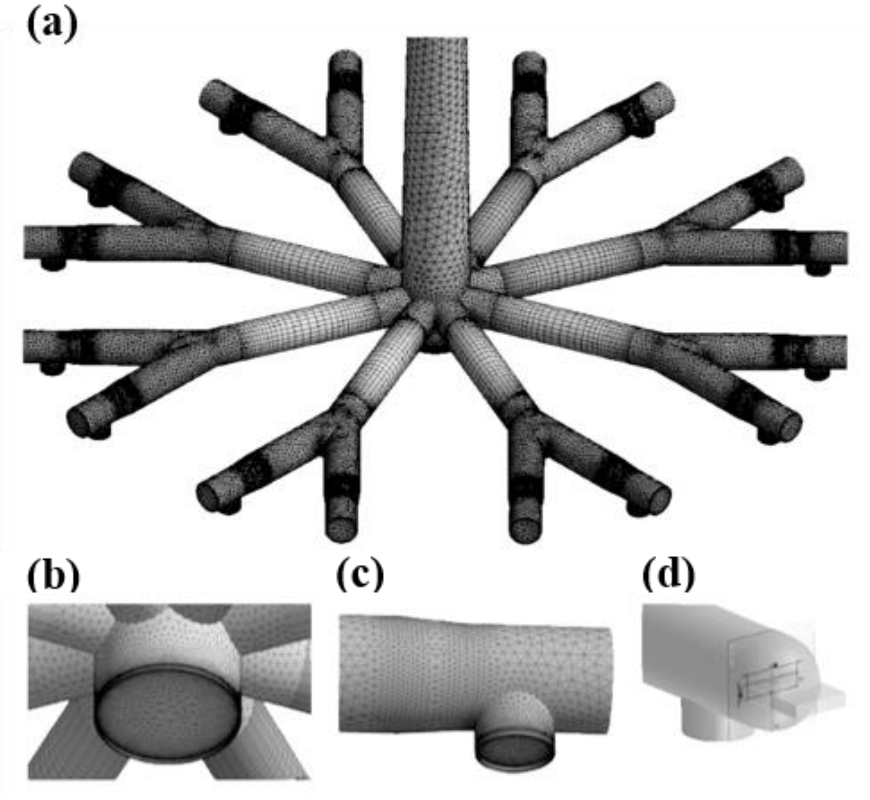

Figure 2.2 (a) Model and meshing for simulation (b) Intersection of first runners (c) End of second runner (d) Shape of gates

second runners, subsequently, it comes out to the gate outlet. We assumed that the mass of each cavity is 5.6 mg, so if the accumulated resin outlet mass flow of each outlet reaches 5.6 mg, we assumed the cavity is completely filled. The number of elements is approximately 2.5 million. There are air vents at the end of the intersection and the second runners, and the thickness of those vents is 50 μm. They can be observed in Figures 2.2(b) and 2.2(c). Moreover, we placed the gates at each end of the second runners and the shape of these gates is shown in Figure 2.2(d). The gates are rectangular in shape and the width is 1.26 mm.

2.3 Boundary conditions

Figure 2.3 shows the boundary conditions used in the simulations. In actual process for manufacturing multi-system micro injection mold, it is hard to make all runners and gates in exactly same size. And these errors can affect the flow of resin polymer which causes cavity filling deviation. In addition, keeping all runners at the same temperature is not an easy process so there can be small differences in the temperature of each runner. These small differences in temperature can have a significant effect on the behavior of polymer, so it can be the major factor for the cavity filling deviation. Therefore, we used the following three primary factors that cause cavity filling deviation: mold temperature, runner diameter, and gate size. The mixed condition illustrated in Figure 2.3(d) is the combination of the mold temperature case and the runner diameter case. The boundary conditions of this mixed condition are described in Table 2.2. and the reason for using this combination without the gate size case will be explained in the result section. We set the reference boundary conditions same as general process conditions for manufacturing micro lens and give variety to other conditions. The range of runner diameter and gate size are same as the errors in actual process, but we exaggerated the runner temperature boundary conditions for simulation convenience in comparison with the actual process. In actual process, the range of runner temperature is in less than 2K.

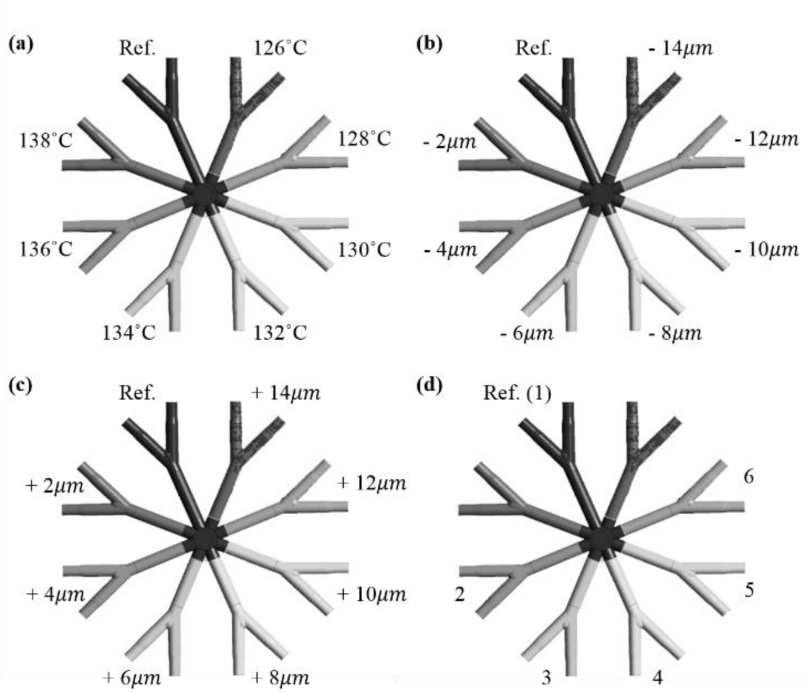

z

Figure 2.3. Boundary conditions for our simulation **(a)** Mold temperature case (reference temperature is 140°C) **(b)** Runner diameter case (reference diameter is 2.3 mm) **(c)** Gate thickness case (reference thickness is 0.3 mm) **(d)** mixed condition (reference mold temperature is 140°C and reference runner diameter is 2.3 mm)

Table 2.2 Boundary conditions for complex case

No.	1	2	3
Conditions	Original condition (140°C, 2.3 mm)	Wall Temperature -4°C Runner diameter -4μm	Wall Temperature -6°C Runner diameter -6μm
No.	**4**	**5**	**6**
Conditions	Wall Temperature -8°C Runner diameter -8μm	Wall Temperature -10°C Runner diameter -10μm	Wall Temperature -12°C Runner diameter -12μm

2.4 Numerical results

2.4.1 Mold temperature variation

First, in Figure 2.4, the outlet mass flow rate of the resin is presented. There are deviation between each outlet mass flow rate and it means flux into each cavity is apt to have deviation when mold temperature of each runner is different. The dotted-line box in this figure refers to the time when each cavity is completely filled. Therefore, the start line of the dotted-line box is the time when the first cavity is completely filled, and the end line of that box is the time when the last cavity is completely filled. The width of the box refers to the difference in time when the first and the last cavity is completely filled, and we call it "filling time delay." If the width of the box is broader, it means filling time delay is longer. And it also indicates that cavity filling deviation is big. Further, the time deviation when each flow front reaches the gate outlet can be observed, and this reach time has also a slight irregular deviation in mold temperature case.

When the first cavity is completely filled, we named the filling rate of other cavities at that time as "filling fraction," and it is presented in Figure 2.5. The square dots in this figure represent the delay time: cavity filling time differences between the first cavity and each subsequent cavity. So, the biggest delay time is the same as the filling time delay. The numerical results that can represent cavity filling deviation is shown in Table 2.3.

Table 2.3 Numerical results of wall temperature case

Wall Temperature (°C)	Cavity Filling Time (ms)	Filling Time Delay (ms)	Filling Fraction
128	229.06	4.27	0.69
130	228.44	3.65	0.72
132	226.66	1.87	0.85
134	224.79	0	1
136	224.79	0	1

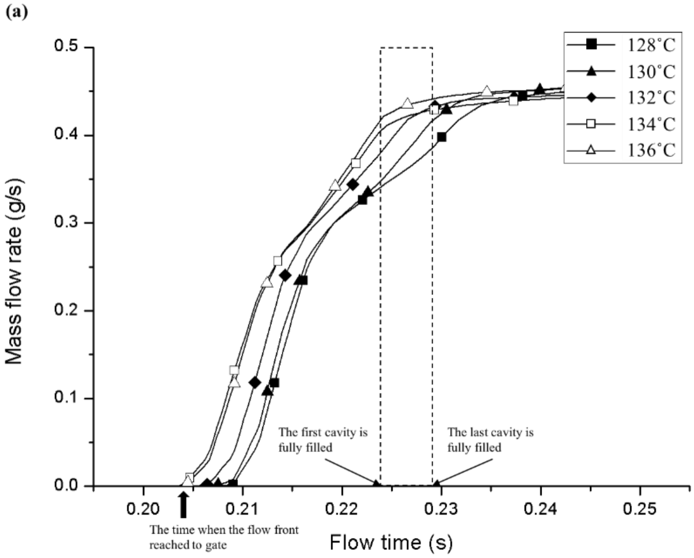

Figure 2.4 Outlet mass flow rate of each runner in wall temperature case

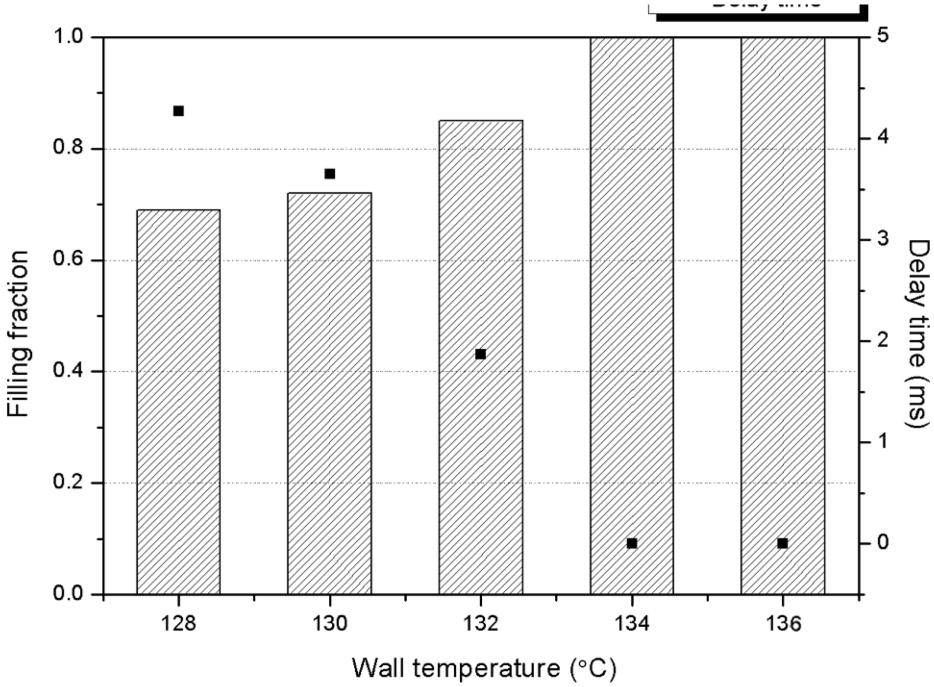

Figure 2.5 Filling fraction and filling time delay of each runner in wall temperature case

2.4.2 Runner diameter variation

The outlet mass flow rate of runner diameter case is shown in Figure 2.6. The result of the outlet mass flow rate shows a similar tendency with the mold temperature case however the time when each flow front reaches the gate outlet has more regular deviation as compared with the mold temperature case. It is because the mold temperature of each runner affects each other at the intersection of first runners, in contrast of the runner diameter case.

Figure 2.7 shows the filling fraction and filling time delay of the runner diameter case and the numerical values of those are shown in Table 2.4. Compared to the mold temperature case, The diameter deviation between each runner seems to be less

Table 2.4 Numerical results of runner diameter case

Runner diameter (μm)	Cavity Filling Time (ms)	Filling Time Delay (ms)	Filling Fraction
-10	258.44	3.11	0.74
-8	257.53	2.2	0.81
-6	256.91	1.58	0.87
-4	256.44	1.11	0.90
-2	255.71	0.38	0.97
Ref.	255.33	0	1

the boundary condition of the mold temperature case is exaggerated for simulation effective to cavity filling deviation than the mold temperature deviation. However, convenience in comparison with the actual process: The error range of mold temperature is $3K$ or less in actual process. However, the error range of runner diameter is $10 \sim 17\mu m$ in actual process so this boundary condition of runner diameter case is similar to the actual process. Thus, the runner diameter variation is more effective to cavity filling deviation than the mold temperature variation.

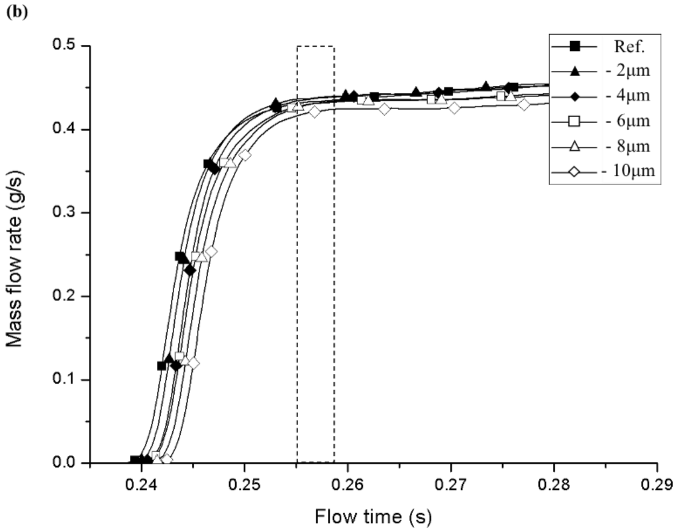

Figure 2.6 Outlet mass flow rate of each runner in runner diameter case

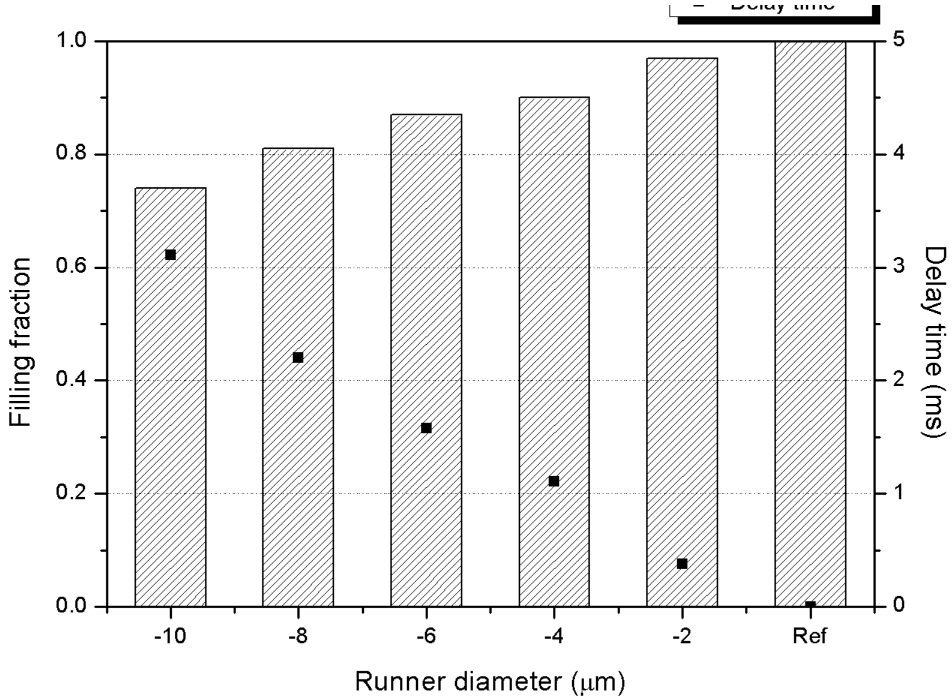

Figure 2.7 Filling fraction and filling time delay of each runner in runner diameter case

2.4.3 Gate thickness variation

Figure 2.8 shows the outlet mass flow rate of gate thickness case. Filling fraction and filling time delay of this case is shown in Figure 2.9 and the numerical result is shown in Table 2.5. Compared to the previous two cases, the gate thickness variation has little effect on cavity filling deviation. Therefore, we conclude that the gate thickness variation is not a major process condition which affects cavity filling deviation and combined the mold temperature case and runner diameter case, for the mixed condition.

Table 2.5 Numerical results of gate thickness case

Gate thickness (μm)	Cavity Filling Time (ms)	Filling Time Delay (ms)	Filling Fraction
+12	234.79	1.43	0.9
+10	234.37	1.01	0.93
+8	234.12	0.84	0.94
+6	234.04	0.68	0.95
+4	233.84	0.48	0.97
Ref.	233.36	0	1

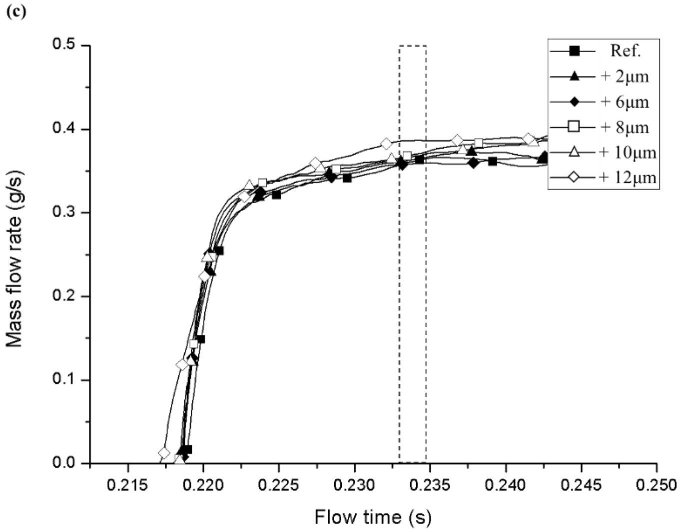

Figure 2.8 Outlet mass flow rate of each runner in gate thickness case

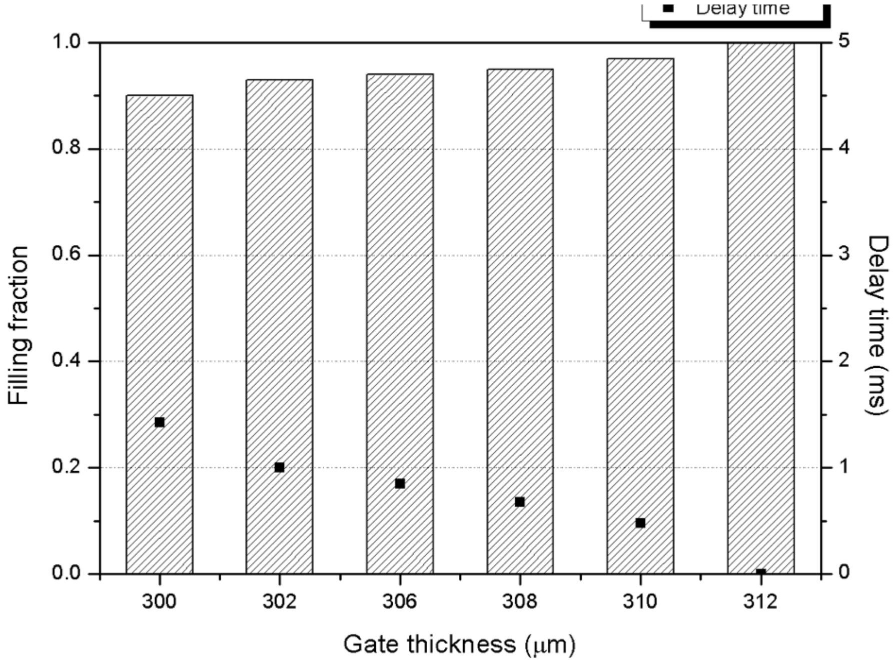

Figure 2.9 Filling fraction and filling time delay of each runner in gate thickness case

2.4.4 Mixed condition

As mentioned earlier, the mixed condition is combination of the mold temperature condition and the runner diameter condition. Figure 2.10 shows the outlet mass flow rate of mixed condition case. The numerical result is shown in Table 2.6.

As expected, the complex case has the worst filling uniformity. This case had the smallest filling fractions and delay times on every boundary condition in comparison to other cases. First, we thought that the condition number 6 would have the smallest filling fraction and delay time, However, the condition number 5 has the worst results in cavity filling. The reason that the condition number 5 has the worst results is because the runner in condition number 6 was affected by the neighboring runner

Table 2.6 Numerical results of mixed condition

Condition No.	Cavity Filling Time (ms)	Filling Time Delay (ms)	Filling Fraction
6	253.52	3.76	0.69
5	253.75	3.99	0.67
4	253.04	3.28	0.72
3	251.69	1.93	0.83
2	250.66	0.9	0.92
1 (Ref.)	249.76	0	1

(the other side of runner with condition number 5) which has high temperature: we do not observe that neighboring runner, but the mold temperature of that runner is set as same as the reference condition.

For comparison, we put the results of all cases together in Figure 2.11. The specific boundary conditions for Figure 2.11 is shown in Table 2.7. The numerical values regarding the filling time delay and the highest filling fraction difference of all cases are shown in Table 2.8. The filling fraction difference was 33% and filling time delay was 3.99ms in the mixed condition case. For the boundary conditions of robust designs for reducing cavity filling deviation, we used this mixed condition.

Table 2.7 Boundary conditions for results in figure 8

No.	1	2	3
Wall temperature case	-10°C	-8°C	-6°C
Runner diameter case	-10μm	-8μm	-6μm
Complex case	Wall Temperature -10°C Runner diameter -10μm	Wall Temperature -8°C Runner diameter -8μm	Wall Temperature -6°C Runner diameter -6μm
No.	4	5	
Wall temperature case	-4°C	Ref.	
Runner diameter case	-4μm	Ref.	
Complex case	Wall Temperature -4°C Runner diameter -4μm	Ref.	

Table 2.8 Filling time delay and biggest filling fraction difference of each case

Simulated Cases	Wall temperature	Runner diameter	Gate size	Complex condition
Filling time delay	3.65ms	3.11ms	1.43ms	3.99ms
Biggest filling fraction difference	28%	26%	10%	33%

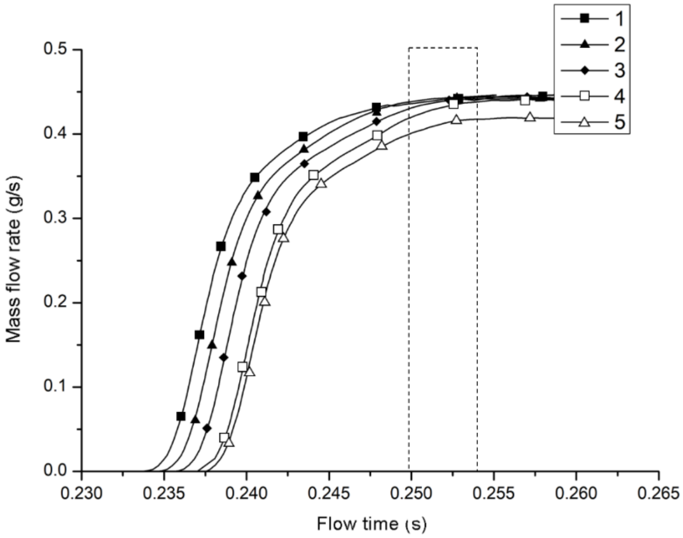

Figure 2.10 Outlet mass flow rate of each runner in mixed condition

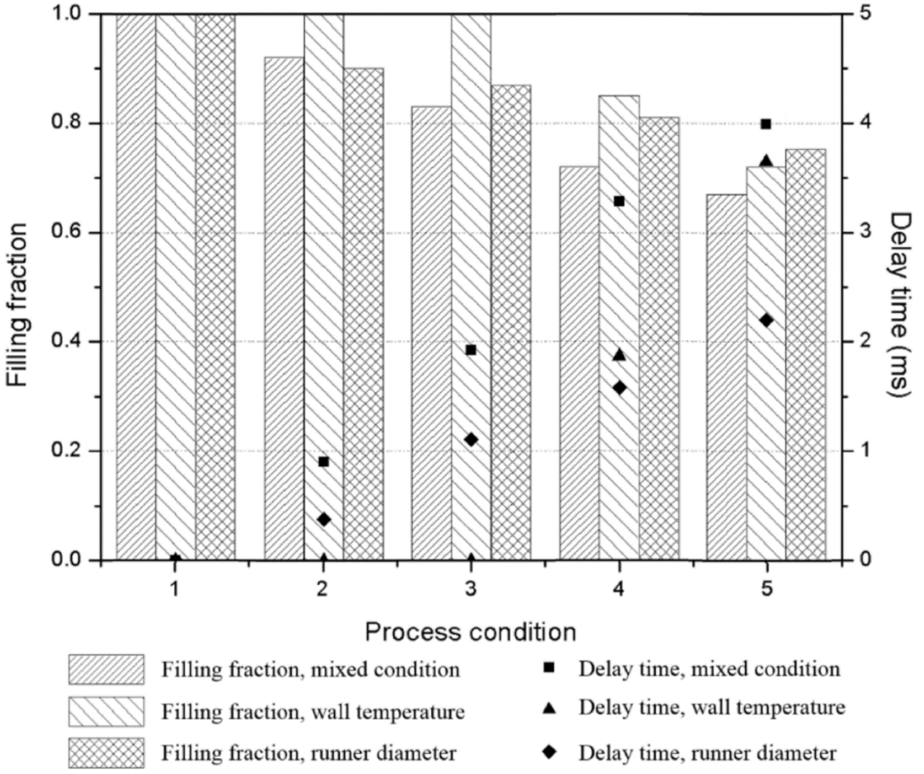

Figure 2.11 Filling fraction and filling time delay of each case

2.5 Robust designs for reducing cavity filling deviation

To reduce cavity filling deviation we simulated and suggested three new models – convergent runner model, reservoir model, and complex model, which is the combination of the other two models. The geometry of these models is described in Figure 2.12. Figure 2.12(a) and (b) are the convergent runner model, (c) is the reservoir model. Using the three models, we calculated their effects on reducing cavity filling deviation. For comparison, we used boundary conditions of the complex case that we simulated, as mentioned earlier.

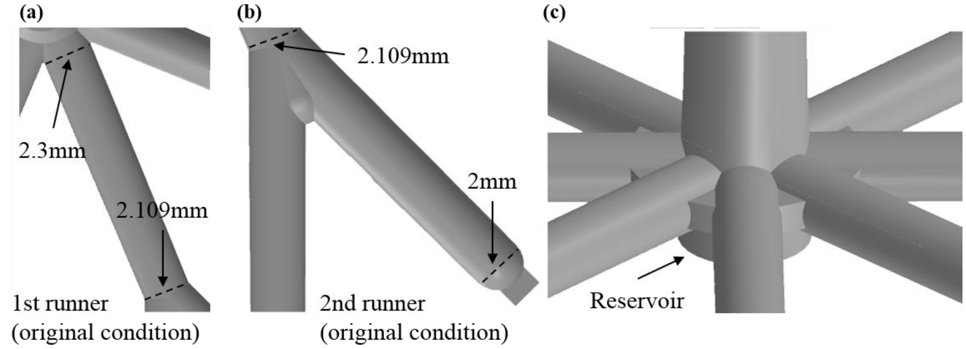

Figure 2.12 Geometry of robust designs **(a)** and **(b)** Convergent runner model **(c)** Reservoir model

2.5.1 Convergent runner model

2.5.1.1 Head loss effect

In order to demonstrate the effectiveness of the robust model, we considered the head loss of a convergent channel. Head loss is defined as the energy loss by friction between the fluid and wall. The head loss in a channel with variable cross-sectional area is given by

$$\Delta h = \int_L \pi d \tau_w dl = \int_L \frac{32\mu Q}{d^2} dl$$

where h is the head loss, τ_w is the shear stress at the wall surface, l is the length of the runner, μ is the viscosity of fluid, Q is the flux, and d is the diameter of the runner. For a convergent channel, the head loss grows non-linearly with the distance. This is in contrast to the case of a channel with constant cross-section as illustrated in Figure 2.13. As the flow front in the runner goes downstream, due to the increased head loss, the speed of flow front slows down. Therefore, even if there exists a difference in the flow front location among runners in the beginning, this difference tends to become smaller as the flow front advances in the convergent runner.

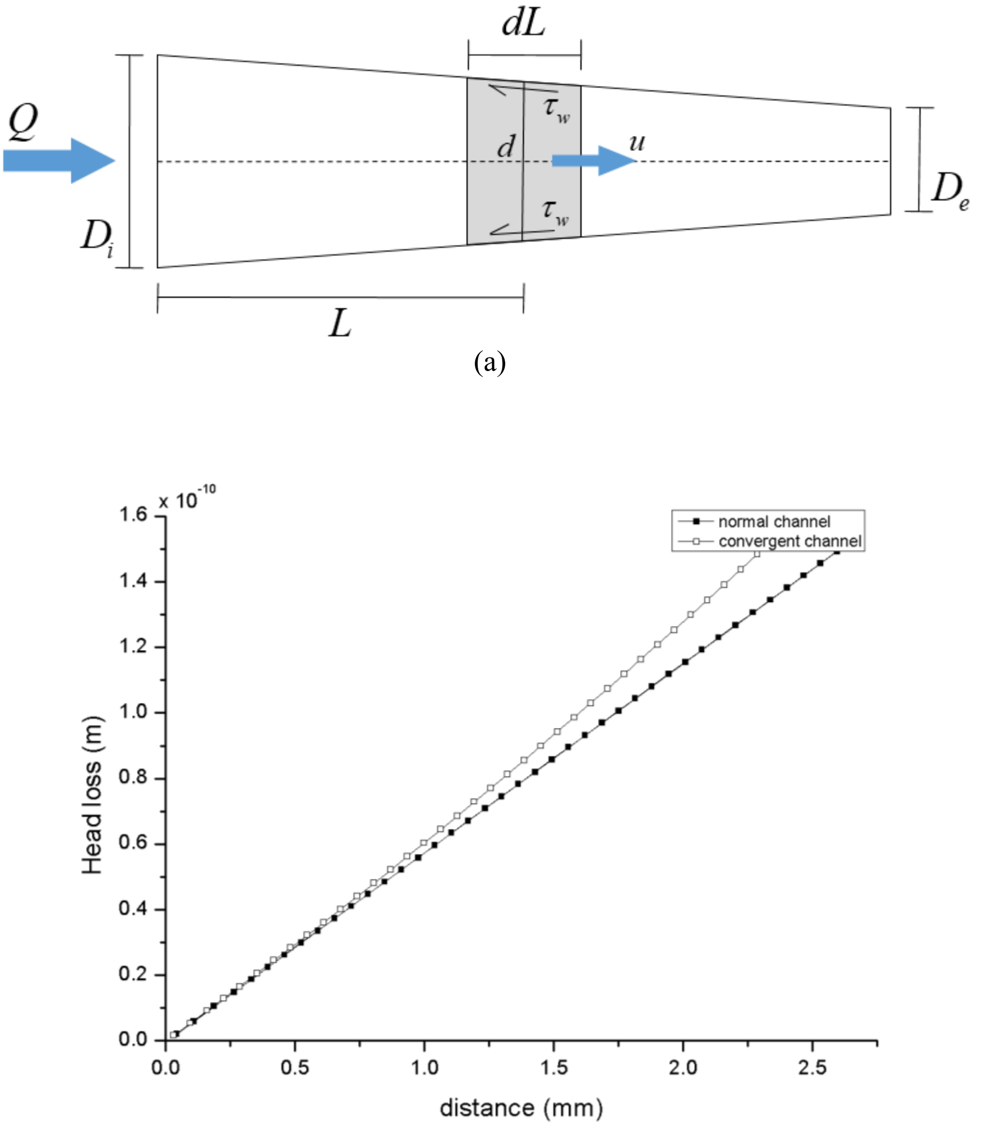

(a)

(b)

Figure 2.13 (a) Basic concept of head loss (b) Head loss increase comparison between normal channel and convergent channel

2.5.1.2 Results of convergent runner model

For the convergent runner model, we set the diameter of every end of the second runners as 2 mm and changed the diameter of the entrance of each first runners same as the complex case in the previous simulation, which subsequently rendered all runners convergent. The diameters of the entrance of the first runners and the second runners are shown in Table 2.9. The numbers of runners are shown in Figure 2.14. The boundary conditions regarding wall temperature are same as the complex case.

The effect of the convergent runner model is summarized in Figure 2.15 and Figure 2.18. Figure 2.15 shows the outlet mass flow rate of convergent runner model. Filling fraction and filling time delay of this case is shown in Figure 2.18 and the numerical result is shown in Table 2.10.

In the convergent model, there exists a new interval (0.225 ms–0.232 ms) when the deviation between the outlet mass flow of each gate decreases. After that time, the deviation increases again, but when we consider the mass of the cavity (5.6 mg), all cavities are fully filled before the difference of flux increases more than the normal channel model. Subsequently, the cavity filling deviation in convergent channel is reduced in comparison to normal channel. Moreover, the arrival time of the flow front to the gate and the difference between each runner decreased. Compared with the result of the original complex case, the deviation of the arrival time and cavity filling time decreased by 62% and 48%, respectively. Also, the largest filling fraction deviation decreased by 20%.

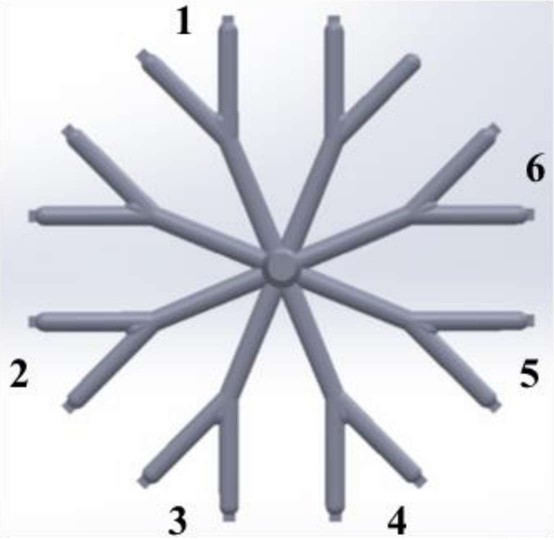

Figure 2.14 The numbers of runners in convergent runner model

Table 2.9 Runner diameters of convergent runner model

Runner No.	1 (Ref.)	2	3	4	5	6
1st runner inlet diameter (mm)	2.300	2.296	2.294	2.292	2.290	2.288
2nd runner inlet diameter (mm)	2.109	2.108	2.107	2.106	2.105	2.105

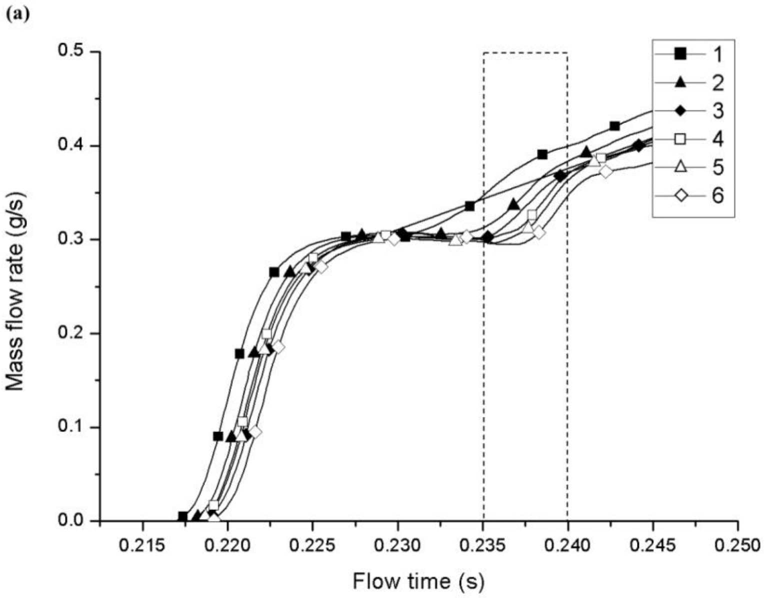

Figure 2.15 Outlet mass flow rate of each runner in convergent runner model

Table 2.10 Numerical results of convergent runner model

Condition No.	Cavity Filling Time (ms)	Filling Time Delay (ms)	Filling Fraction
Ref. (1)	236.29	0	1
2	237.41	1.11	0.93
3	238.33	2.04	0.87
4	238.10	1.81	0.89
5	238.38	2.09	0.87
6	239.16	2.87	0.83

2.5.2 Reservoir Model

For the reservoir model, we introduced the reservoir on the first runner intersection of our system. The diameter of this reservoir was 7.8 mm and the thickness was 0.5 mm. The boundary conditions of the reservoir model were same as the complex case.

The effect of the reservoir model is summarized in Figure 2.16 and Figure 2.18. Figure 2.16 shows the outlet mass flow rate of convergent runner model. Filling fraction and filling time delay of this case is shown in Figure 2.18 and the numerical result is shown in Table 2.11.

In the reservoir model, there is similar interval (where the deviation between outlet mass flow of each gate decreases) with regards to the convergent model in 0.224 ms–0.232 ms. After that time, the deviation between the outlet mass flow was more stable than the convergent model. The deviation of the arrival time and the cavity filling time decreased by 48% and 46%, respectively, and the highest filling fraction difference decreased by 18% in comparison to the original complex boundary condition. It is because the resin flow pooled into the reservoir until it reached a certain amount. Subsequently, the flows with similar amount proceeded from the reservoir through each runner. Further, the reservoir shortened the runner length which had non-uniformity, and it made the resin flow stable.

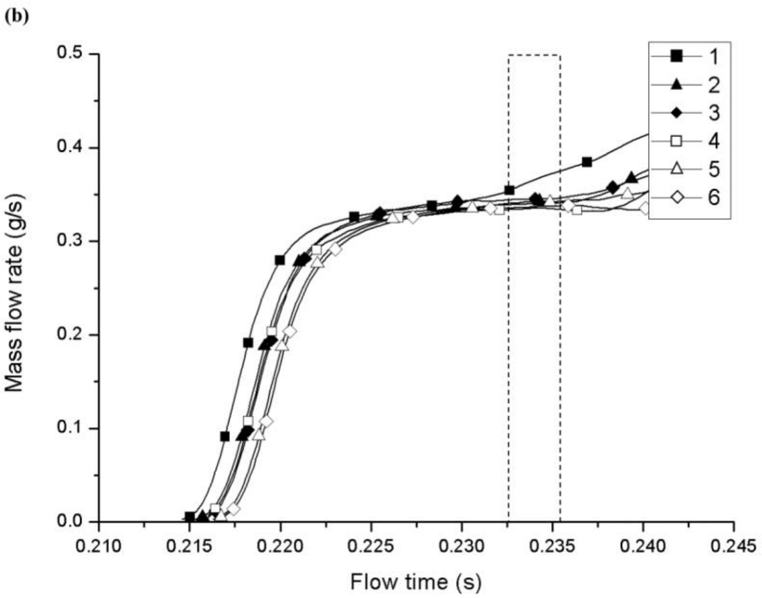

Figure 2.16 Outlet mass flow rate of each runner in reservoir model

Table 2.11 Numerical results of reservoir model

Condition No.	Cavity Filling Time (ms)	Filling Time Delay (ms)	Filling Fraction
Ref. (1)	232.90	0	1
2	234.03	1.13	0.92
3	234.09	1.19	0.92
4	234.40	1.5	0.9
5	235.06	2.16	0.85
6	235.33	2.43	0.84

2.5.3 Complex model

In former two robust models, the effect of those in reducing cavity filling deviation was confirmed. Thus, we assumed that we can reduce cavity filling deviation more if we combine those two models. For that reason, we made the complex model combined with the convergent runner model and the reservoir model. The boundary conditions are same as former two cases.

The outlet mass flow rate of complex model is shown in Figure 2.17 and the numerical result is shown in Table 2.12. The summarized results of filling fraction and filling time delay for our all three robust models are shown in Figure 2.18. For the complex model, the most stable outlet mass flow was observed, the arrival time was the fastest, and the deviation between each runner was the smallest. The deviation of the arrival time, cavity filling time, and the highest filling fraction difference decreased by 60%, 62%, and 22%, respectively, and this was the best result obtained from our models as our assumption.

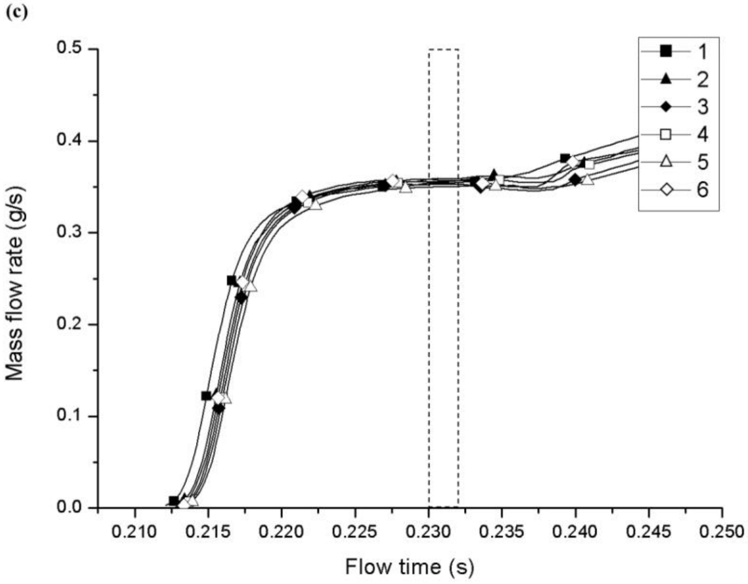

Figure 2.17 Outlet mass flow rate of each runner in complex model

Table 2.12 Numerical results of complex model

Condition No.	Cavity Filling Time (ms)	Filling Time Delay (ms)	Filling Fraction
Ref. (1)	230.03	0	1
2	230.59	0.56	0.96
3	230.99	0.96	0.93
4	231.10	1.07	0.92
5	231.55	1.52	0.89

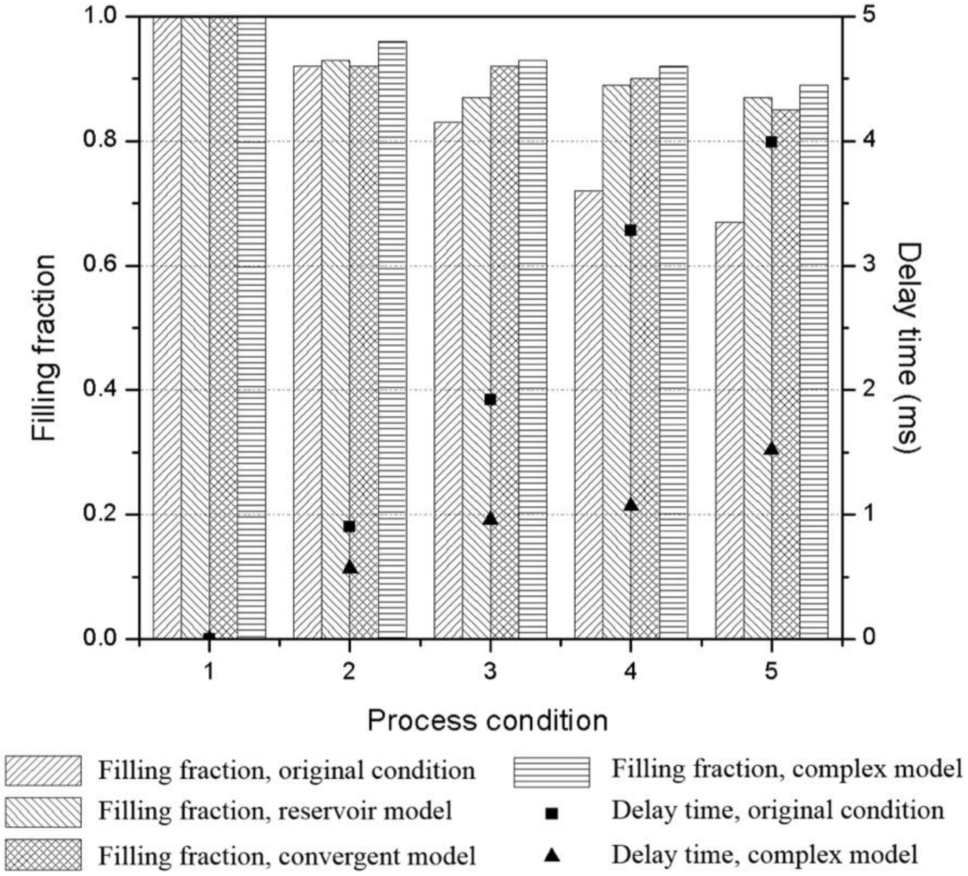

Figure 2.18 Filling fraction and filling time delay of each robust design model

Chapter 3

Analysis on flow mark

3 Analysis on flow mark

Flow mark is one of the typical defects in micro-injection molding. When the hot melted polymer is injected into the relatively colder mold, the rheological behavior of polymer near the mold wall can make the defect like flow mark. There are former studies that changing some process conditions can reduce these flow marks. [12-17] We tried to find the major process conditions that affect to the generation and the size of the flow mark by multilateral analysis.

As mentioned earlier, there are some hypotheses that try to explain the mechanism how flow marks generate. We choose “Go-Over” hypothesis introduced by Yoshii et al [12] and did parametric study for finding the major process conditions and investigated the relation between the size of flow mark and these major process conditions. We verified the results of parametric study by experimental analysis and CFD simulations.

3.1 Parametric study

We performed the parametric study for generation of flow mark in order to find the relation between the major processing conditions and size of flow mark.

There is general agreement that an increase in injection velocity leads to a reduction in flow mark size and the thickness of vitrified layer seems to be proportional to flow mark size. That is to say, the thicker vitrified layer, the bigger flow mark depth. [12-17]

Thus, we modeled the growth of the vitrified layer behind the contact line of melted resin and mold wall, and we investigated the relation between the major process conditions and flow mark size. So, we regarded the depth of flow mark as the function of vitrified layer thickness as follows:

$$\begin{aligned} d_{depth} &= function(\delta_v) \\ &= function\left(\delta_v\left(T_m, T_r, \alpha_r, V_{avg}\right)\right) \\ &= function(T_m, T_r, \alpha_r, V_{avg}) \end{aligned}$$

where $d_{depth}, \delta_v, T_m, T_r, \alpha_r$ and V_{avg} represent the depth of flow mark, the vitrified layer thickness of contact line, the mold temperature, the melted resin temperature, the thermal diffusivity of resin and the average velocity of flow front, respectively. and we assumed that the thickness of vitrified layer as the primary parameter which is the most significant term for generation of flow mark. The approaches later is as follows [12, 15, 17, 27, 28].

When the hot melted polymer is injected into the mold cavity, the melted polymer with the low thermal diffusivity right behind the contact line of resin and mold wall starts to cool the instant it contacts the mold wall. For the conceptual model, we assumed that the heat transfer between the polymer and the mold is considered to be one-dimensional. and we neglect heat transfer by convection at the flow front of polymer because it is much smaller than that by conduction. Then, we can describe

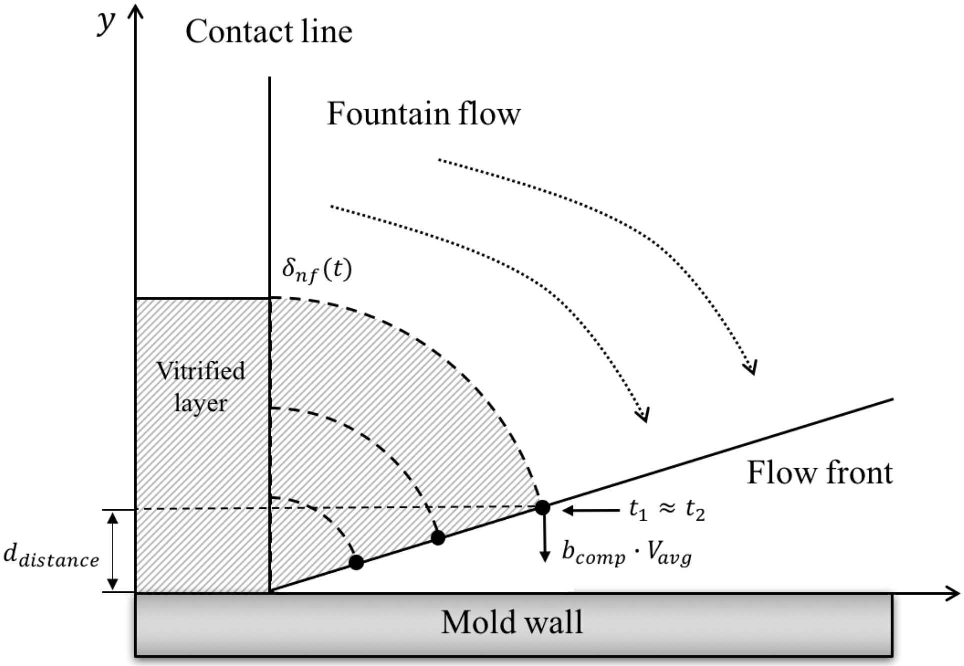

Figure 3.1 Analysis model for generation of flow mark

the temperature distribution $T(y, t)$ of the resin as a problem of transient heat conduction in semi-infinite slab with initial temperature T_m(the mold temperature) and T_r(the resin temperature) based on the analysis model shown in Figure 3.1.

When the melted polymer contacts the mold wall, the temperature of the resin-mold contact interface T_i can be expressed as follows:

$$T_i = \frac{b_r \cdot T_r + b_m \cdot T_m}{b_r + b_m} \tag{3.1}$$

where, b_r and b_m are the thermal effusivities of resin and mold, respectively. The thermal effusivity b is defined as follows:

$$b = \sqrt{\rho \cdot c_p \cdot k} \tag{3.2}$$

where ρ, c_p and k are density, specific heat and thermal conductivity, respectively.

Then, we can express the temperature distribution of melted polymer at the contact line as:

$$\frac{T(y,t) - \ T_i}{T_r - T_i} = erf\left(\frac{y}{2\sqrt{\alpha_r \cdot t}}\right) \tag{3.3}$$

where α_r is the thermal diffusivity of polymer, as mentioned earlier. the thermal diffusivity is defined as follows:

$$\alpha = \sqrt{\frac{k}{\rho \cdot c_p}} \tag{3.4}$$

erf denotes the Gauss error function, and it defines as follows:

$$erf(\eta)=\frac{2}{\sqrt{\pi}}\int_0^{\eta} e^{x^2}dx \quad (3.5)$$

For express the thickness of vitrified layer, we let T be the no-flow temperature T_{nf}, in which the polymer can't flow. And we considered T_{nf} as glass transition temperature of the resin polymer. Then the equation 3.3 can be rewritten by

$$\frac{T_{nf}-T_i}{T_r-T_i}=erf\left(\frac{\delta_{nf}}{2\sqrt{\alpha_r\cdot t}}\right) \quad (3.6)$$

In the boundary conditions for our experiments, $\frac{T_{nf}-T_i}{T_r-T_i}$ is around 0.6 or smaller than 0.6. In this case, as described in Figure 3.2, the right term of equation 3.6 with gauss function can be assumed that:

$$\frac{T_{nf}-T_i}{T_r-T_i}=erf\left(\frac{\delta_{nf}}{2\sqrt{\alpha_r\cdot t}}\right)\cong\frac{\delta_{nf}}{2\sqrt{\alpha_r\cdot t}} \quad (3.7)$$

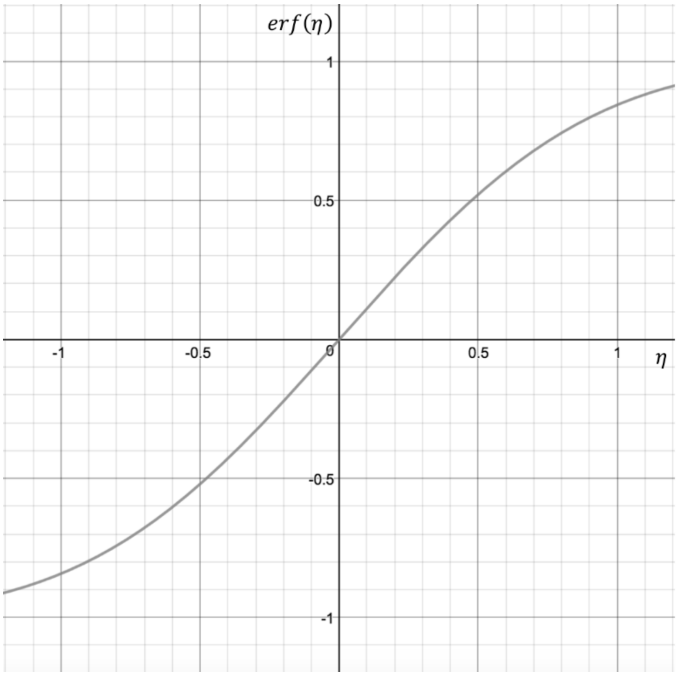

Figure 3.2 Gauss error function

If we let the left term of equation 3.7 as dimensionless temperature θ_{nf}, the thickness of vitrified layer at the contact line δ_{nf} can be described as follows:

$$\delta_{nf}(t) = 2\theta_{nf}\sqrt{\alpha_r \cdot t} \tag{3.8}$$

$$\theta_{nf} = \frac{T_{nf} - T_i}{T_r - T_i}$$

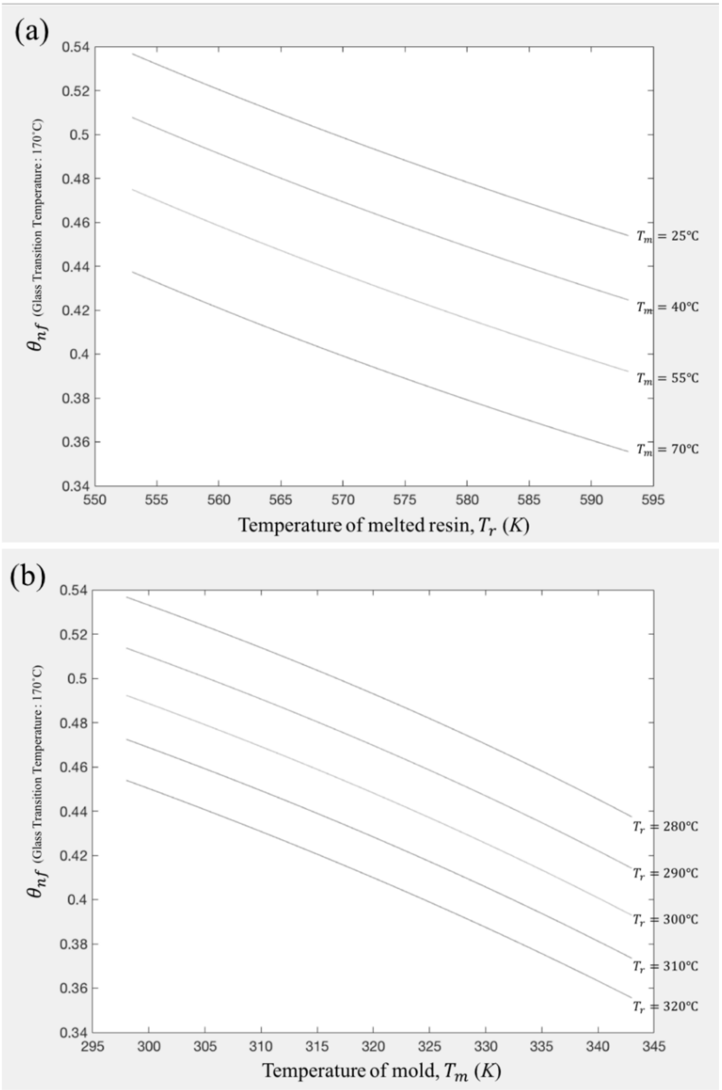

Figure 3.3 Relation between theta and two major process temperature (a) temperature of melted resin (b) temperature of mold wall

In Figure 3.3, the relations between θ_{nf} and the temperature of mold and melted polymer are shown. As the figure describes, θ_{nf} is inversely proportional to the temperature of mold and melted polymer.

In order to find how the flow marks generate, we supposed follow process as hypothesis for flow mark generation. First, in Figure 3.1, the semi-circles from the contact line mean the propagation line of the vitrified layer beginning with contact line of flow front when flow front comes into contact with the mold wall. We set the time t_1 which take for temperature at certain point of flow front to reach T_{nf}, and the time t_2 which takes for the point of flow front at the same position as that of t_1 to contact the mold wall. When flow front is advancing, close to the contact line, the flow front is vitrified because it is affected by the cool down of temperature. However, when $t_1 \geq t_2$ due to the effect of the fountain flow at the advancing free surface, the flow front will go-over the vitrified layer and flow mark generates under that point. So we propose that the flow mark size is proportional to the thickness of vitrified layer in such a condition as $t_1 \cong t_2$.

$$t_1 = \frac{{\delta_{nf}}^2}{4{\theta_{nf}}^2 \cdot \alpha_r} \tag{3.9}$$

$$t_2 = \frac{d_{distance}}{b_{comp} \cdot V_{avg}} \tag{3.10}$$

$$\delta_{nf} = 2\theta_{nf} \cdot \sqrt{\frac{d_{distance} \cdot \alpha_r}{b_{comp} \cdot V_{avg}}} \tag{3.11}$$

$$Depth\ of\ flowmark \sim \delta_{nf} = 2\theta_{nf} \cdot \sqrt{\frac{d_{distance} \cdot \alpha_r}{b_{comp} \cdot V_{avg}}} \qquad (3.12)$$

$$\theta_{nf} = \frac{T_{nf} - T_i}{T_r - T_i}$$

where $d_{distance}$ is the distance between a point of flow front and mold wall, b_{comp} is the velocity fraction of flow front in the direction of thickness and V_{avg} is the average velocity of flow front, respectively. We regarded that $d_{distance}$ and b_{comp} are constant at the flow front near the mold wall in all conditions.

According to the equation 3.12 and Figure 3.3, the ways to decrease flow mark size are as follows:

a. A high temperature for the mold, T_m

b. A high temperature for the melted polymer, T_r

c. A high average velocity of flow front (high injection velocity), V_{avg}

Thus, if we use the same polymer for experiments, the three major process conditions that we choose have some relations with the size of flow mark and this is in a full agreement with most of the published experimental data in the literatures. [12-17]

3.2 Experimental analysis on flow mark

For verifying the results from parametric study, we did some experiments. As follows the parametric study, we choose three major process conditions: injection velocity, resin temperature and mold temperature. We investigated the depth and the width of flow marks on the sample made by micro-injection molding process with changing those three major process conditions.

3.2.1 Material for experiments

Polycarbonate, also known as PC, is a thermoplastic polymer used commonly for injection molding process. With its advantage in strength, toughness and optical transparency in some grades, PC has a wide variety of applications including electronic components, data storage, security components, et cetera.

In this study, LUPOY GP1000M (PC, LG Chemical) is used for experimental material. Figure 3.4 and Figure 3.5 show the VT (Volume-Temperature) and viscosity properties of PC. Thermaophysical properties of this material is shown in Table 3.1. For convenience of observation, we used material mixed with black dye.

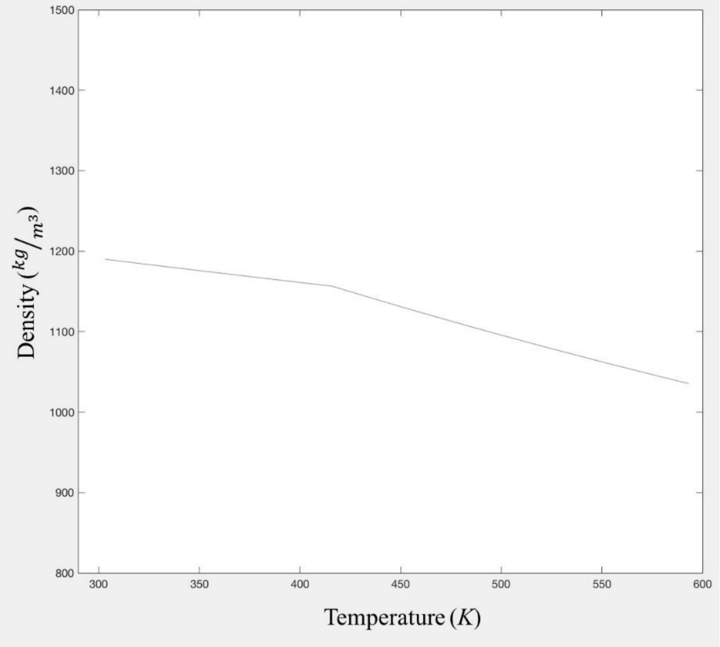

Figure 3.4 Volume-Temperature graph of used polymer(LUPOY)

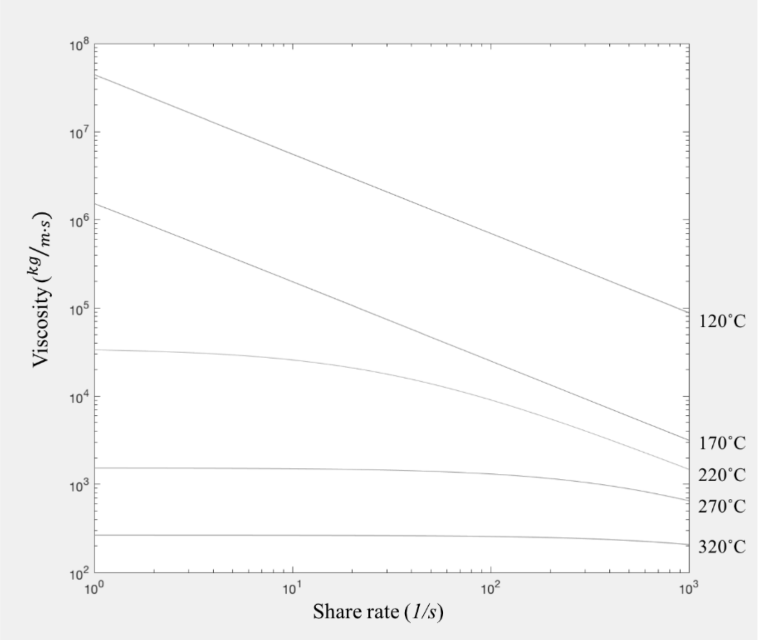

Figure 3.5 Viscosity curves of used polymer (LUPOY)

Table 3.1 Thermophysical properties of LUPOY

Injection temperature	Above 280℃
Glass transition temperature	170℃
Specific heat	1866 J/kg · K
Thermal conductivity	0.184 W/m · K

3.2.2 Instrumentals for experiments

3.2.2.1 Injection molding machine

The all electric injection molding machine SE50D (Sumimoto, Japan) was used for experiments. Diameter of screw is 20mm and capacity limit of injection molding is 51cm^3. Maximum clamping force is 50 Ton and maximum distance between tie bar is 35cm. The heating system is attached around the screw, so the temperature of melted resin can be controlled. Figure 3.6 Shows the picture of this machine and Table 3.2 shows the specification of this machine.

Table 3.2 Specification of injection molding machine

Injection molding machine SE50D (Sumimoto)	
Machine dimensions $(L \times W \times H)$	$3631\text{mm} \times 984\text{mm} \times 1670\text{mm}$
Clamping force	50tonf
Screw diameter	20mm
Injection pressure	$2760\,\text{kgf/cm}^2$
Screw stroke	87mm
Injection speed (max)	500mm/s
Mold space (min – max)	160mm – 350mm

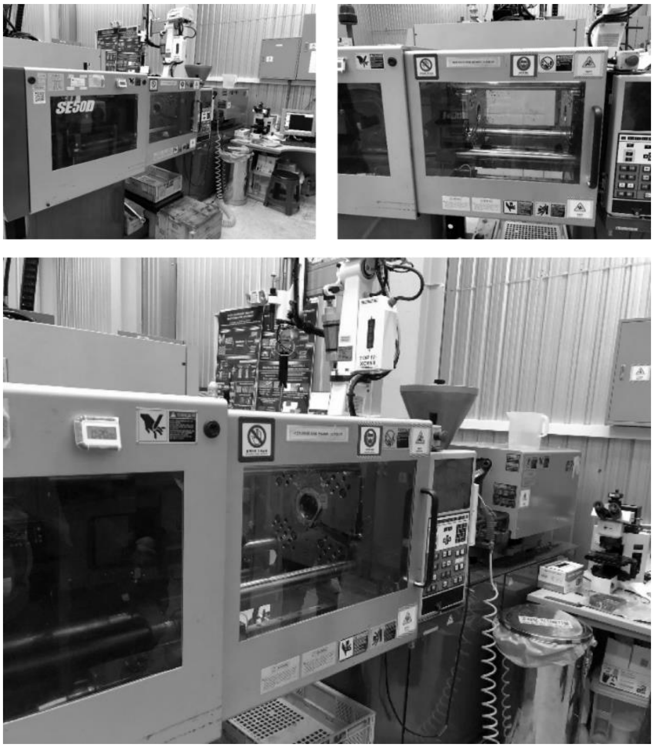

Figure 3.6 Injection molding machine for experiments (SE50D, Sumimoto)

3.2.2.2 Mold specification

The mold for this experiment is made by aluminum. Electric heater is installed beneath the surface of mold cavity, so the mold temperature can be controlled with this system. The shape of cavity is thin cuboid and the length of cavity is $60mm$, the width is $30mm$ and the thickness is $15mm$. The melted polymer is injected into the sprue and it goes through the runner, and fills the cavity consequently. We measured the size of flow mark generated on the surface of the samples made with this mold cavity. The shape of mold is shown in Figure 3.7 and the sample product made by this mold is shown in Figure 3.8.

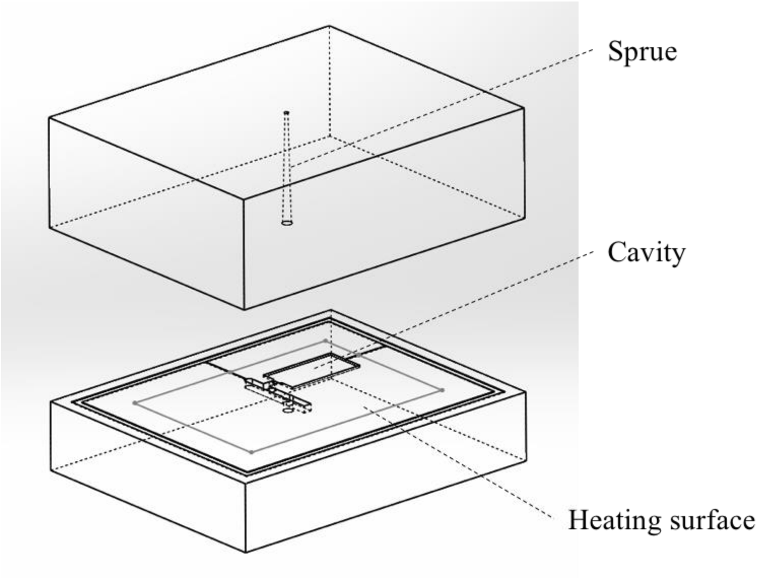

Figure 3.7 The Schematic illustration of mold for the experiments

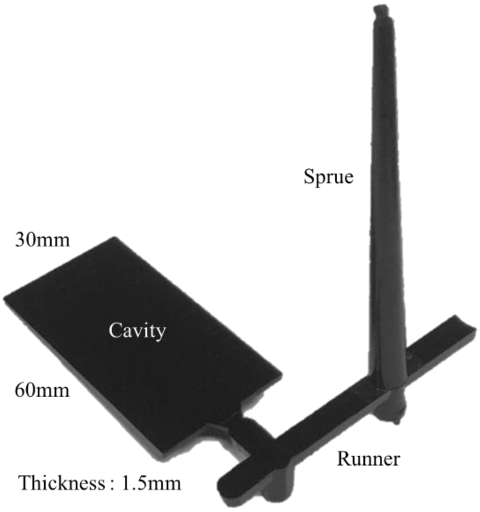

Figure 3.8 The sample made by the mold used for the experiments

3.2.3 Measurement of flow mark

For measurement of flow mark size, we used stylus 2D profiler. Stylus 2D profiler supports 2D measurements of step height, roughness, bow and more. The system scratches on the surface of sample with tiny stylus and observes the form of surface in 2D and measures height or roughness.

In this study, we used Alpha step D-500 from KLA-Tencor for alpha step instrument. The range of step height is from nanometers to $1200\mu m$ and the range of low force is from $0.03mg$ to $15mg$. The picture of this machine is shown in Figure 3.9.

Figure 3.10 is 3D surface of the sample observed by confocal laser microscope. We measured the depth and the width of 20 flow marks in the position of 30mm from the gate and averaged it.

Figure 3.9 Stylus 2D profiler (Alpha step P-500, KLA-Tencor)

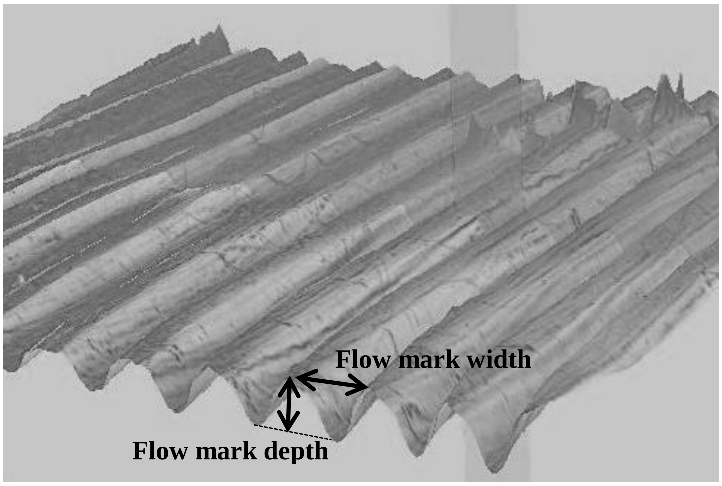

Figure 3.10 3D surface of the sample

3.2.4 Process conditions

As mentioned earlier, we considered injection speed, resin temperature and mold temperature as major process conditions related to generation of flow mark and size of flow mark. Thus, we did our flow mark experiments with changing those three process conditions. The specific process conditions are described in Table 3.3.

Table 3.3 Process conditions for the flow mark experiments

Variations	Conditions					Notes
Injection Speed (mm/s)	2.5	5	7.5	10	12.5	Resin T = 280, 290, 300˚C Mold T = 25˚C
Resin Temperature (℃)	280	290	300	310	320	Resin T = 280˚C Injection V = 5, 7.5 mm/s
Mold Temperature (℃)	25	40	55	70		Resin T = 280˚C Injection V = 5, 7.5, 10 mm/s

3.2.5 Results of experimental analysis

The results by experiments showed the size of flow mark generated near mold wall under the various process conditions.

First, the effect of injection speed is shown in Figure 3.11 and Figure 3.12. The depth of flow mark by changing injection speed is shown in Figure 3.11 and the width is shown in Figure 3.12. According to the equation 3.12, an increase in injection speed (the flow front velocity) will reduce the size of flow mark and the results of experiment also showed the same tendency. When the injection speed was above $12.5mm/s$, the flow mark was barely generated and when the resin temperature was increased, the size of flow mark was decreased in all conditions of changing injection speed.

The effect of resin temperature is shown in Figure 3.13 and Figure 3.14. The depth of flow mark by changing resin temperature is shown in Figure 3.13 and the width is shown in Figure 3.14. According to the equation 3.12 and Figure 3.3(a), an increase in resin temperature will reduce the size of flow mark and the results of experiment also showed the same tendency. When we increased the injection speed, the size of flow mark was decreased. With $10mm/s$ injection speed, The flow mark was removed when resin temperature was above $300°\mathrm{C}$.

The effect of mold temperature also showed the same tendency. The depth of flow mark by changing mold temperature is shown in Figure 3.15 and the width is shown in Figure 3.16. According to the equation 3.12 and Figure 3.3(b), an increase in mold temperature will reduce the size of flow mark and the results of experiment also showed the same tendency. Especially, the flow mark was barely generated or removed when the mold temperature was above $55°\mathrm{C}$. When we increased the injection speed, the size of flow mark was decreased.

The comparison between the depth of flow marks and δ_{nf}/A in equation 3.12 is shown in Figure 3.17. A is defined as $\sqrt{d_{distance}/b_{comp}}$ in the right term of equation 3.12. As we assumed before in parametric study, the depth of flow marks is proportional to the thickness of vitrified layer. We fitted this relationship in linear function, and the function was:

$$Depth\ of\ flow\ mark = -7.32 \times 10^{-6} + (4.41 \times 10^{-5})\frac{\delta_{nf}}{A}.$$

The result also showed that the depth of flow mark is proportional to the width of flow mark. The relation is shown in Figure 3.18. The relation is well fitted with linear function and the R_{square} is 0.9773.

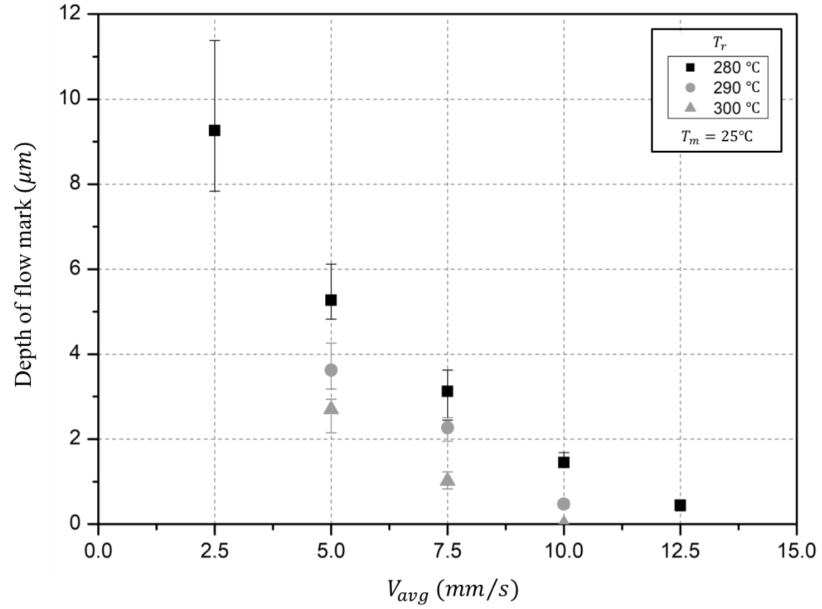

Figure 3.11 The depth of flow mark by changing injection speed (experimental result)

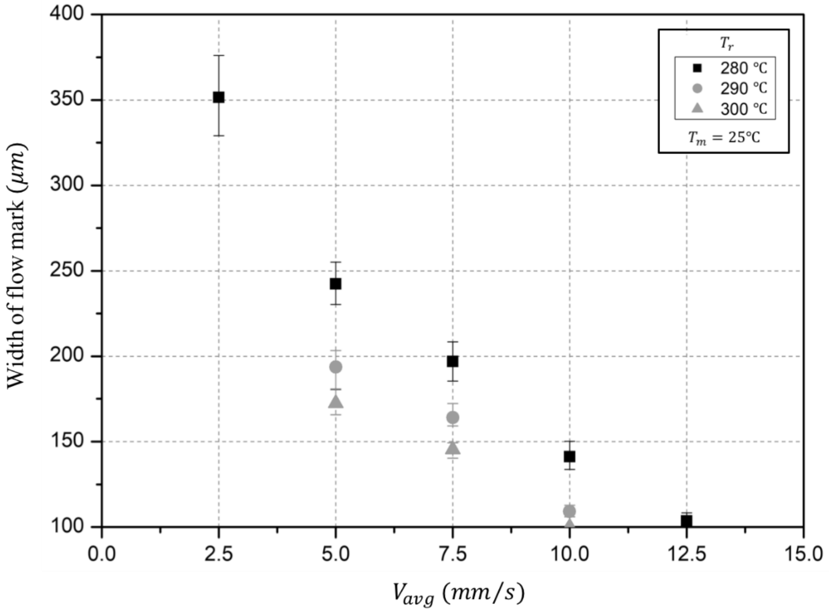

Figure 3.12 The width of flow mark by changing injection speed (experimental result)

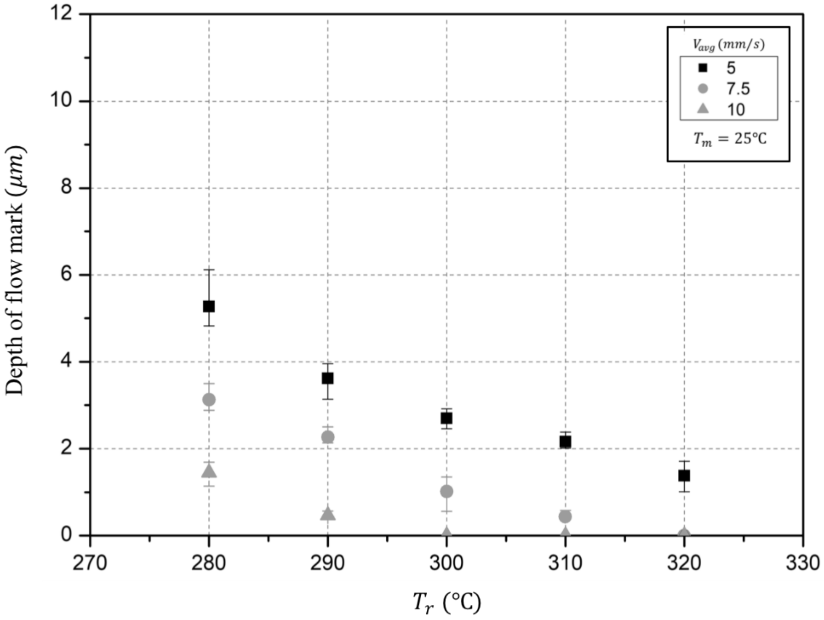

Figure 3.13 The depth of flow mark by changing resin temperature (experimental result)

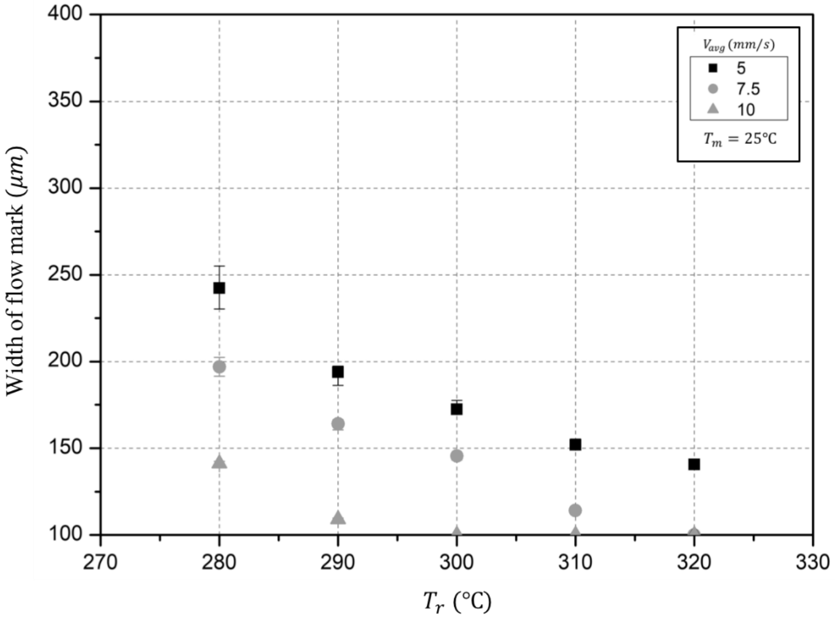

Figure 3.14 The width of flow mark by changing resin temperature (experimental result)

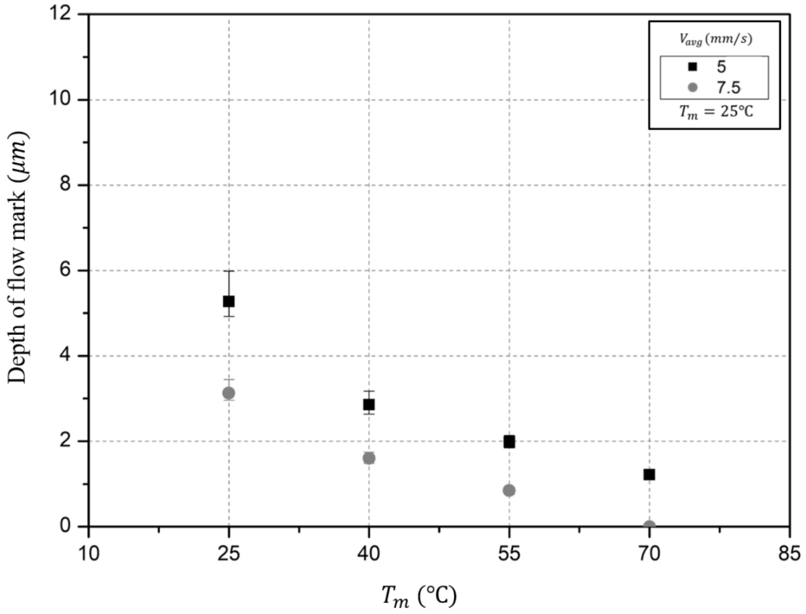

Figure 3.15 The depth of flow mark by changing mold temperature (experimental result)

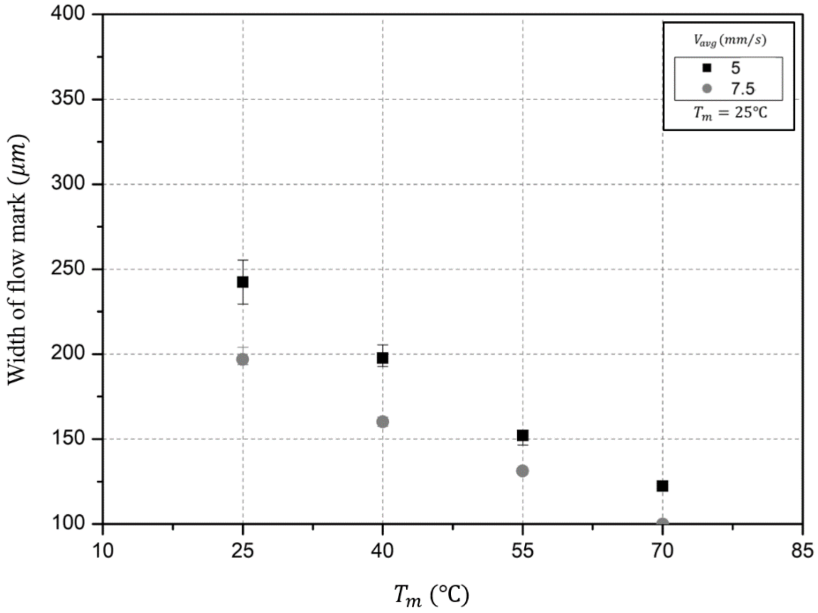

Figure 3.16 The width of flow mark by changing mold temperature (experimental result)

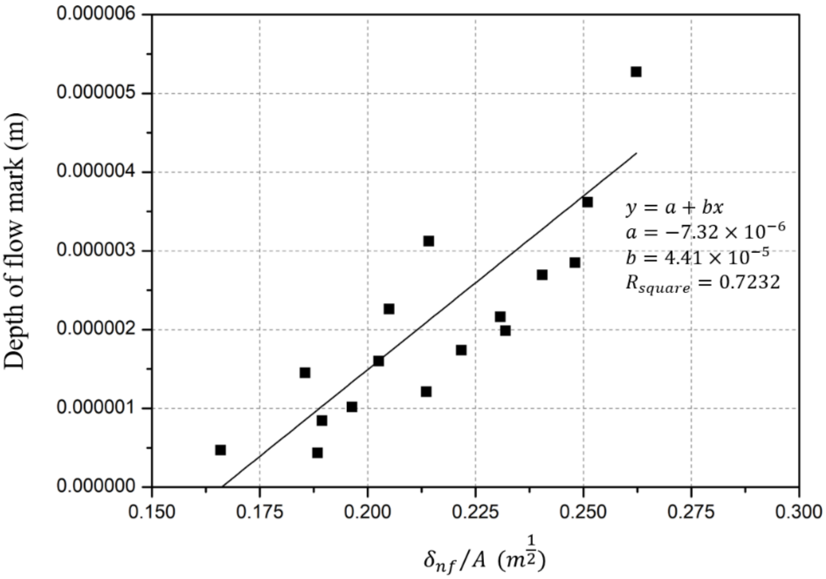

$$A = \sqrt{d_{distance}/b_{comp}} \qquad Depth\ of\ flowmark \sim \delta_{nf} = 2\theta_{nf} \cdot \sqrt{\frac{d_{distance} \cdot \alpha_r}{b_{comp} \cdot V_{avg}}} \qquad \theta_{nf} = \frac{T_{nf} - T_i}{T_r - T_i}$$

Figure 3.17 The relation between the depth of flow marks and $\boldsymbol{\delta_{nf}/A}$ (experimental result)

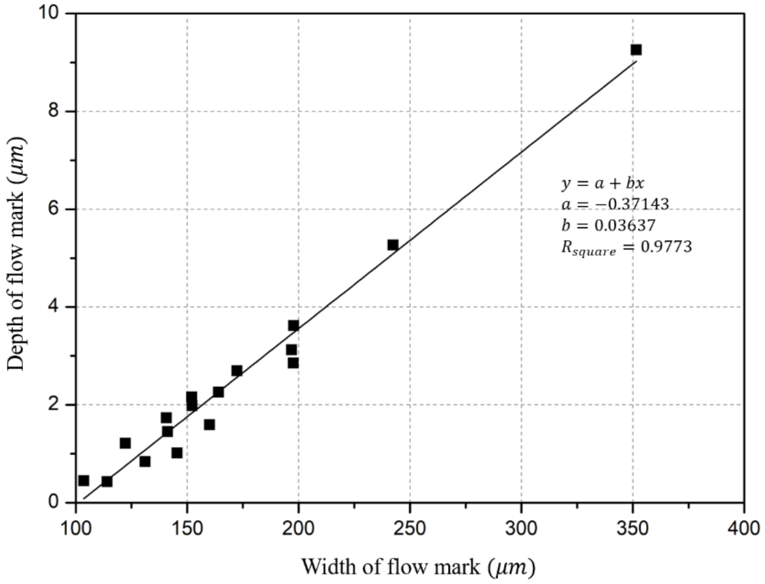

Figure 3.18 The relation between the depth and the width of flow mark (experimental result)

3.3 Numerical analysis on flow mark

We did numerical analysis on flow mark generation. We changed the major process conditions mentioned earlier: injection speed, resin temperature and mold temperature. The generation process of flow mark was also observed with the contour of resin flow in mold cavity model. The size of flow mark generated in CFD simulations is compared with the results of experiments. Basically, we used theories same theories as our former cavity filling deviation analysis for this simulation. Volume of Fluid (VOF) method with Piecewise-Linear Interface calculation (PLIC) method is used for solution algorithm of flow with moving free surfaces. For pressure-velocity coupling scheme, we used Pressure-Implicit with Splitting of Operators (PISO) algorithm.

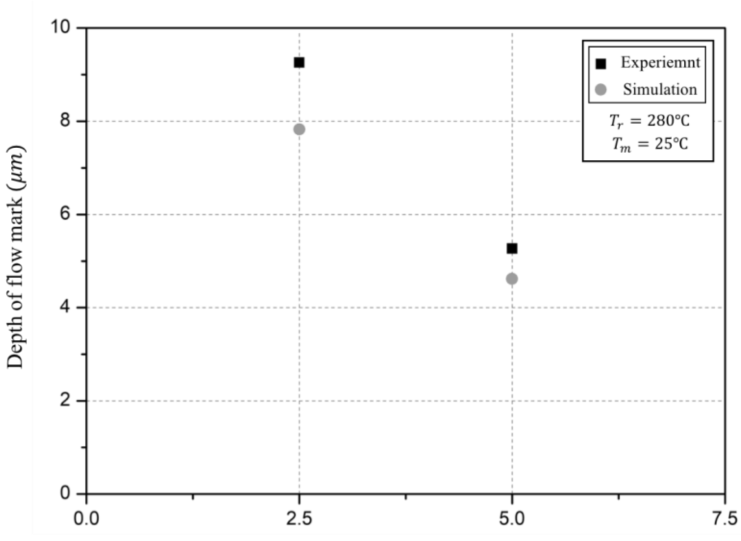

Figure 3.19 The result of numerical analysis comparing to the result of experiment

3.3.1 Validation of numerical analysis

First, we did CFD simulations with the same boundary conditions used in former experiments for validation of numerical analysis. We simulated two cases: 2.5mm/s and 5mm/s for injection speed. Resin temperature was 280°C and mold temperature was 25°C. The result is shown in Figure 3.19. We compared the depth of flow mark obtained by numerical and experimental analysis. The depth of flow mark obtained by CFD simulation was slightly smaller than the result of experiment but it was in similar scale and it showed the same tendency. Thus, we decided to regard the numerical analysis by CFD simulation as reliable. For other numerical analysis, we used the properties of another material for increasing convergence of simulation.

3.3.2 Material properties used in numerical analysis

The Cross-Arrhenius model is adopted with regard to the viscosity of the polymer material. The Cross-Arrhenius model has temperature and shear rate as dependent factors, and the model is given by

$$\eta = H(T)\frac{\eta_0}{1 + (\lambda\dot{\gamma})^{1-n}} \tag{3.13}$$

$$H(T) = exp\left[\alpha\left(\frac{1}{T - T_0} - \frac{1}{T_\alpha - T_0}\right)\right] \tag{3.14}$$

where η_0 is zero-shear-rate viscosity, λ is time, $\dot{\gamma}$ is share rate, and n is power-law index. λ is the inverse of the shear rate where the fluid viscosity changes from Newtonian to power-law behavior. $H(T)$ is the temperature dependence, known as Arrhenius law. α is the ratio of the activation energy to the thermodynamic constant and T_α is a reference temperature for which $H(T) = 1$. T_0 is the temperature shift, and we set it to 0.

For characterizing the specific heat (C_P) and thermal conductivity (k), we used the piecewise-linear method. The piecewise-linear method is described for finding and optimal segment approximation to specified functions from discrete data by a number of connected straight-line segments [25, 26]. For example of specific heat, we set 12 points of specific heat as a function of temperature obtained from the experimental procedures and assumed the values between each point in the neighborhood to be linear. The thermal conductivity is characterized by the same method. We assumed that the properties of air and mold are constants.

we used the thermal characteristic values of EP-7000, the polymer resin in the polypropylene series. The polymer material is assumed to be incompressible. So, the density of the polymer material is constant in the entire simulation process, and its value is given as, $\rho = 1110$ kg/m^3. The Cross-Arrhenius model constants for the viscosity of the polymer material are shown in Table 3.4. Also, the specific heat and thermal conductivity for the polymer material are shown in Figure 3.20 and Figure 3.21, respectively.

Figure 3.22 shows the Cross-Arrhenius model with respect to values in Table 3.4. It indicates the viscosity of the polymer material used in this study based on the temperature and shear rate.

As mentioned before, the property values of the mold material and air are assumed to be constants for convenience of calculation. The density, specific heat, and thermal conductivity of the mold material are 8030 kg/m^3, 502.48 J/kg·K, and 16.27 W/m·K, respectively. Air is considered as an ideal gas, and the density, the specific heat, the thermal conductivity, and the viscosity of air are 1.225 kg/m^3, 1006.43 J/kg·K, 0.0242 W/m·K, and 1.7894×10^{-5} kg/m·s, respectively.

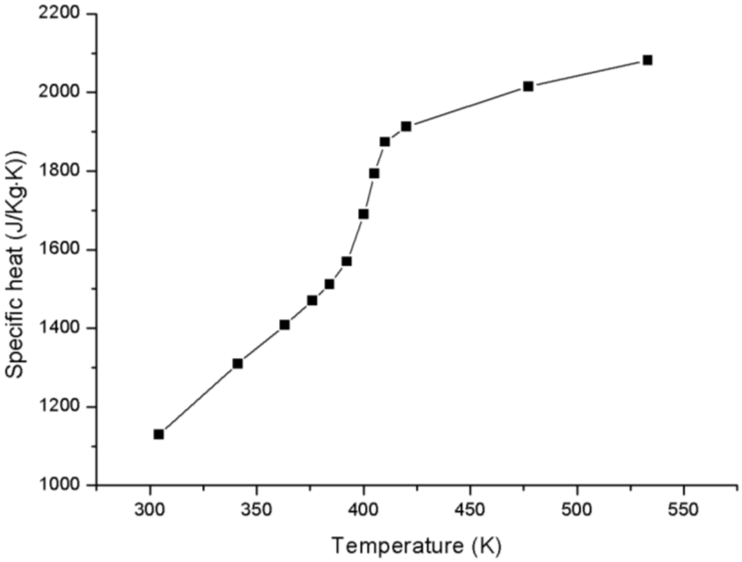

Figure 3.20 Specific heat of the material used in simulation (EP-7000)

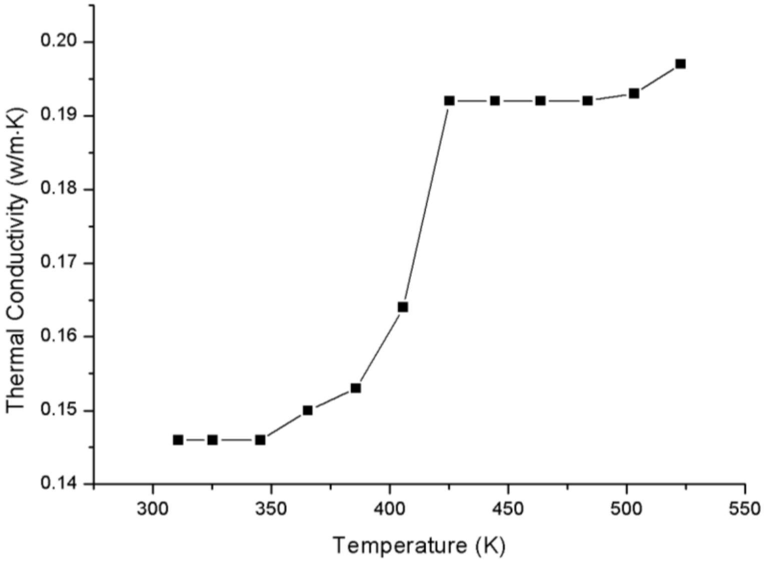

Figure 3.21 Thermal conductivity of the material used in simulation (EP-7000)

Table 3.4 Values used in Cross-Arrhenius model (EP-7000)

Symbol	Value	Unit
η_0	5280	$\mathrm{kg/m \cdot s}$
n	0.269	-
λ	0.009216	s
T_α	530.1209	K
α	17373.33	K

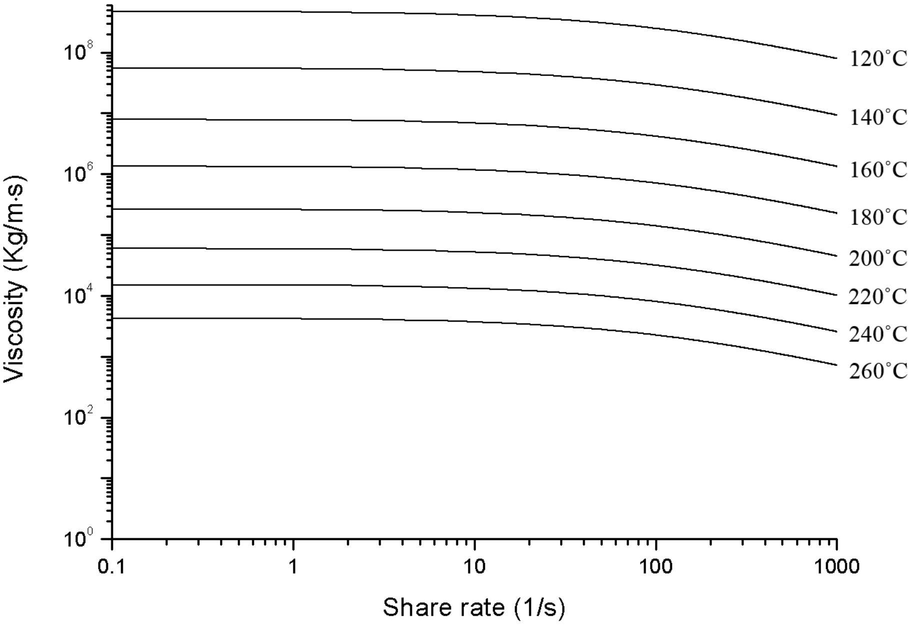

Figure 3.22 Viscosity curves of the material used in simulation using Cross-Arrhenius model (EP-7000)

3.3.3 Modeling and meshing

To observe the flow mark generation in CFD simulation, we considered 2D rectangular cavity model. Figure 3.23 shows the model that we used for our flow mark simulation. The thickness of cavity was $50\mu m$ and the length of cavity was $100\mu m$, respectively. For observing resin flow near the mold cavity wall in more detail, we densify the mesh near the mold cavity wall. The number of elements is approximately 126,000. The orthogonal quality of the mesh was 0.999. Figure 3.24 shows the meshing for our model.

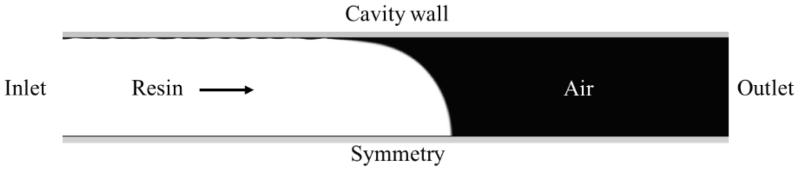

Figure 3.23 Modeling of CFD simulation for flow mark generation

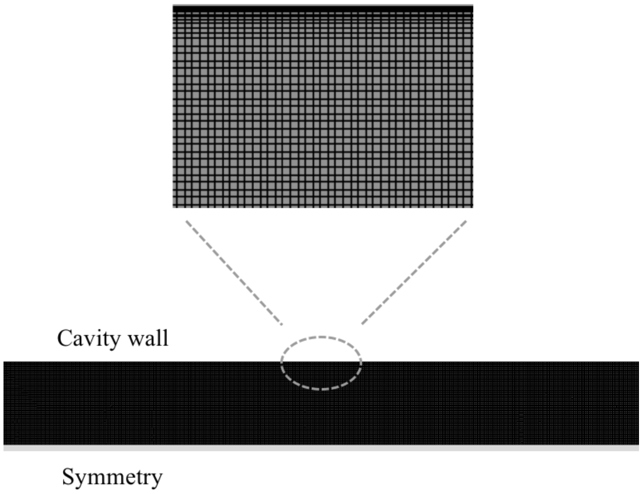

Figure 3.24 Meshing of the model used in CFD simulation for flow mark generation

3.3.4 Measurement of flow mark

For the measurement of flow mark generated in CFD simulation, we made an image processor. With the image processor, we changed the contour of resin flow obtained by CFD simulation to black-and-white image. Then we counted the pixels of flow mark and recalculate the size of flow mark according to the proportion of our model. We averaged 10 flow marks.

3.3.5 Boundary conditions

As mentioned earlier, we considered injection speed, resin temperature and mold temperature as major process conditions related to generation of flow mark and size of flow mark. Thus, we did our flow mark simulations with changing those three boundary conditions. The specific boundary conditions are described in Table 3.5. We used velocity-inlet for inlet condition and outlet-vent for outlet boundary condition.

Table 3.5 Boundary conditions for the flow mark simulations

Validations	Conditions					Notes
Injection speed (m/s)	0.1	0.3	0.5			Resin T = 260˚C Mold T = 90˚C
Resin temperature (℃)	240	260	280			Mold T = 90˚C Injection V = 0.1 m/s
Mold temperature (℃)	90	110	130	150	170	Resin T = 260˚C Injection V = 0.1 m/s

3.3.6 Results of numerical analysis

3.3.6.1 Comparison with "Go-Over" hypothesis

For the validation of "Go-Over" hypothesis and the parametric study we did earlier, we observed the contour of resin flow and moving free surface of flow front. The contour observed when the flow mark was generated is shown in Figure 3.25. It seemed that the flow front from the contact line near the mold is vitrified when the time elapsed, and the resin above that vitrified flow front went over it. Then the flow mark was generated. This flow mark generation process observed by CFD simulation was well fitted with the "Go-Over" hypothesis and our parametric study.

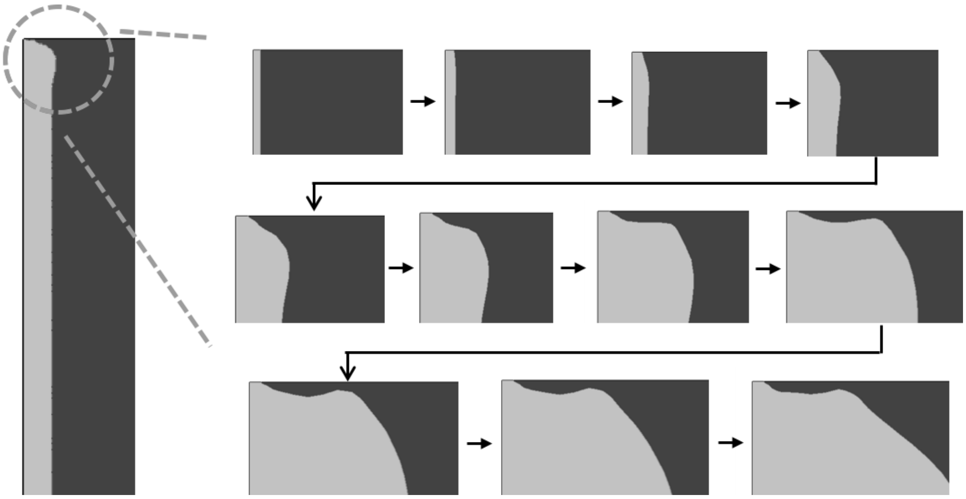

Figure 3.25 The contour observation of flow mark

3.3.6.2 Comparison with experimental results

The results by numerical analysis showed the size of flow mark generated near mold wall under the various process conditions.

First, the effect of injection speed is shown in Figure 3.26 and Figure 3.27, the depth of flow mark and the width of flow mark, respectively. According to the equation 3.12 and the experimental result with changing the injection speed, an increase in injection speed (the flow front velocity) will reduce the size of flow mark. The results of numerical analysis also showed exactly same tendency.

The effect of resin temperature and mold temperature are shown from Figure 3.28 to Figure 3.31. According to the equation 3.12 and the experimental result, increases in those temperature conditions will reduce the size of flow mark. The results of numerical analysis also showed exactly same tendency in both conditions.

The comparison between the depth of flow marks in CFD simulation and δ_{nf}/A in equation 3.12 is shown in Figure 3.32. As we assumed before in parametric study and investigated in the analysis of experimental data, the depth of flow marks is proportional to the thickness of vitrified layer. We also fitted this relationship in linear function, and the function was:

$$Depth\ of\ flow\ mark = \ 1.06 \times 10^{-7} + (6.02 \times 10^{-5})\frac{\delta_{nf}}{A}.$$

The slope and y-intercept in the function of CFD simulation was in similar scale with those of experiments, but they have a little difference. We estimated that these differences in constants is caused by the inner-flow characteristic of each polymer and viscoelastic characteristic of polymer flow.

We also investigated the relation between the depth and the width of flow mark in numerical analysis. The relation is shown in Figure 3.33, and the result also showed that the depth of flow mark is proportional to the width of flow mark as same as experimental result. The relation is fitted with linear function and the R_{square} is 0.8002. The slopes of these linear functions from experimental result and numerical result were in similar.

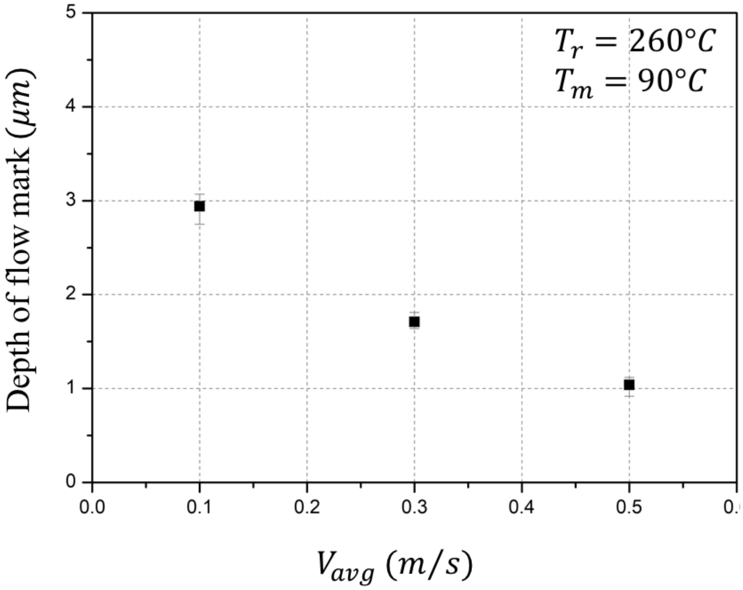

Figure 3.26 The depth of flow mark by changing injection speed (CFD simulation)

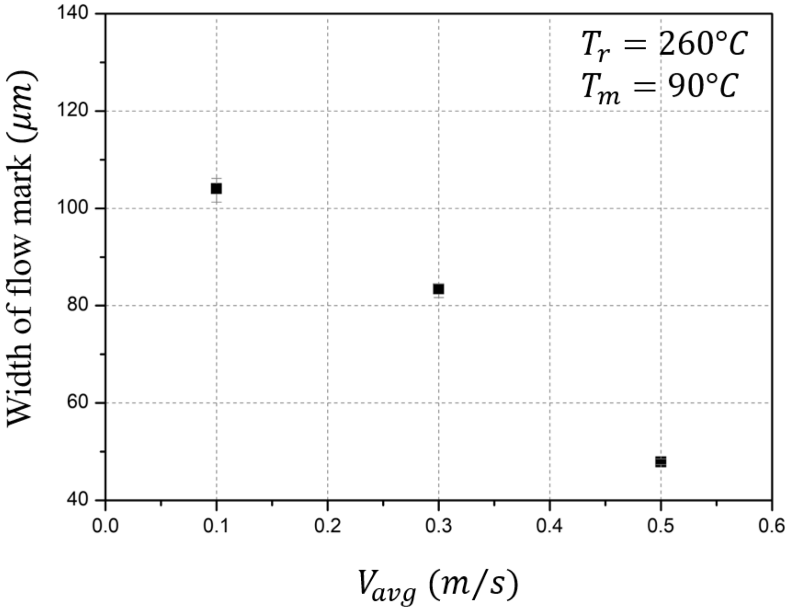

Figure 3.27 The width of flow mark by changing injection speed (CFD simulation)

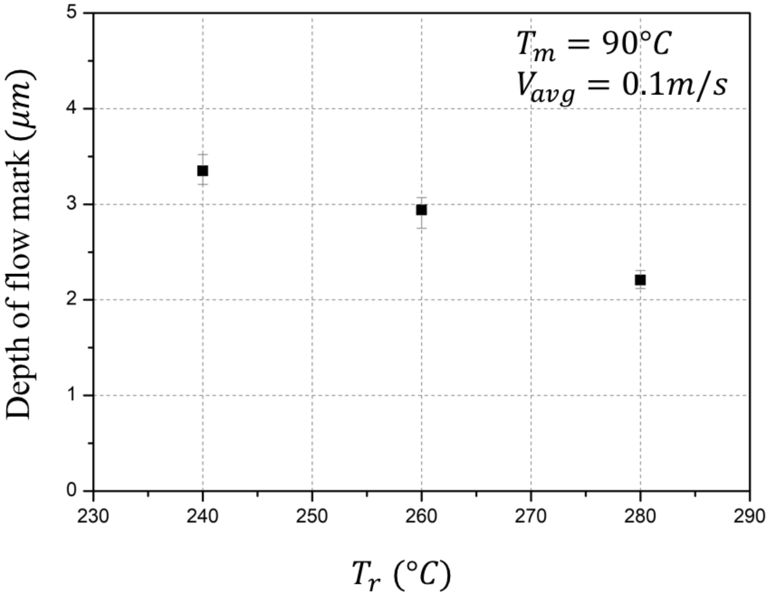

Figure 3.28 The depth of flow mark by changing resin temperature (CFD simulation)

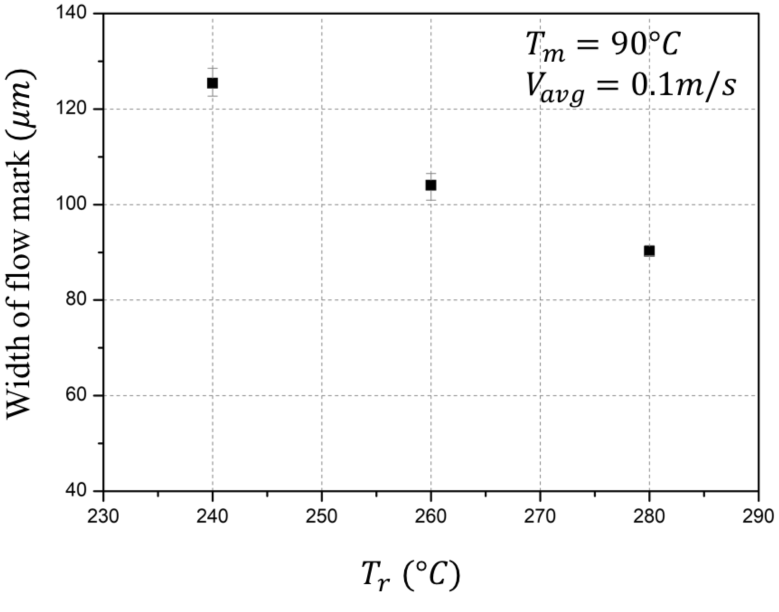

Figure 3.29 The width of flow mark by changing resin temperature (CFD simulation)

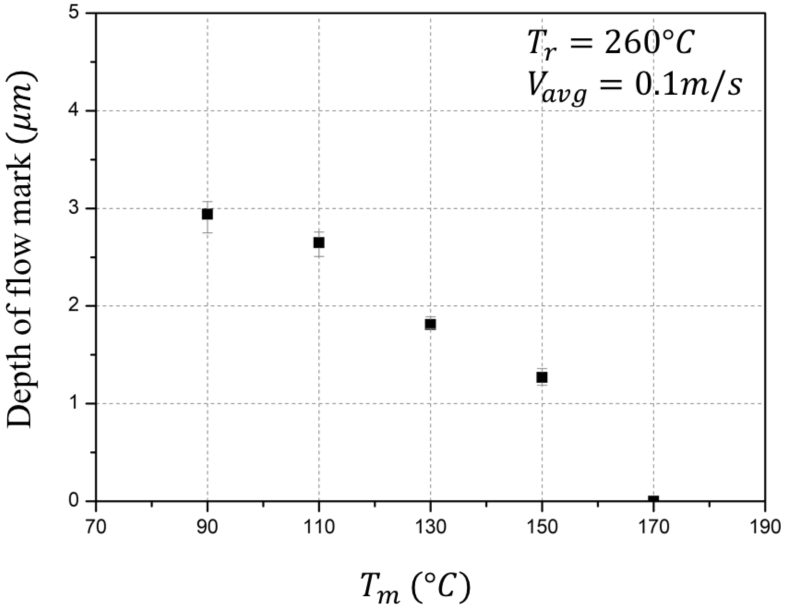

Figure 3.30 The depth of flow mark by changing mold temperature (CFD simulation)

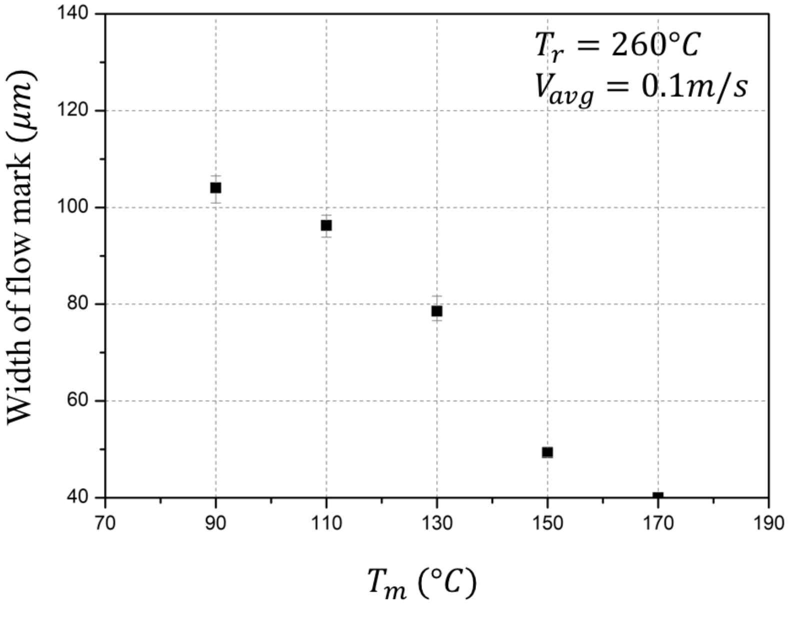

Figure 3.31 The width of flow mark by changing mold temperature (CFD simulation)

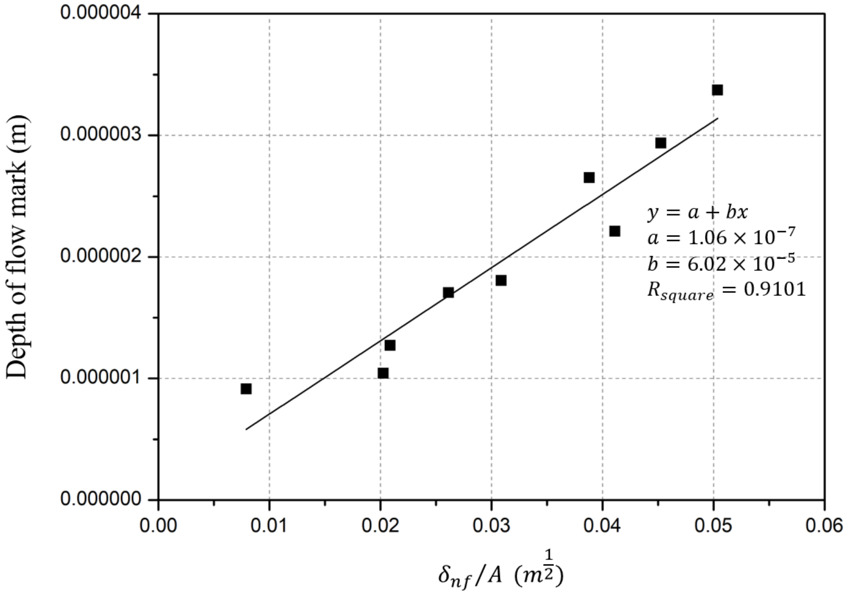

$$A = \sqrt{d_{distance}/b_{comp}} \qquad Depth\ of\ flowmark \sim \delta_{nf} = 2\theta_{nf} \cdot \sqrt{\frac{d_{distance} \cdot \alpha_r}{b_{comp} \cdot V_{avg}}} \qquad \theta_{nf} = \frac{T_{nf} - T_i}{T_r - T_i}$$

Figure 3.32 The relation between the depth of flow marks and $\boldsymbol{\delta_{nf}/A}$ (CFD simulation)

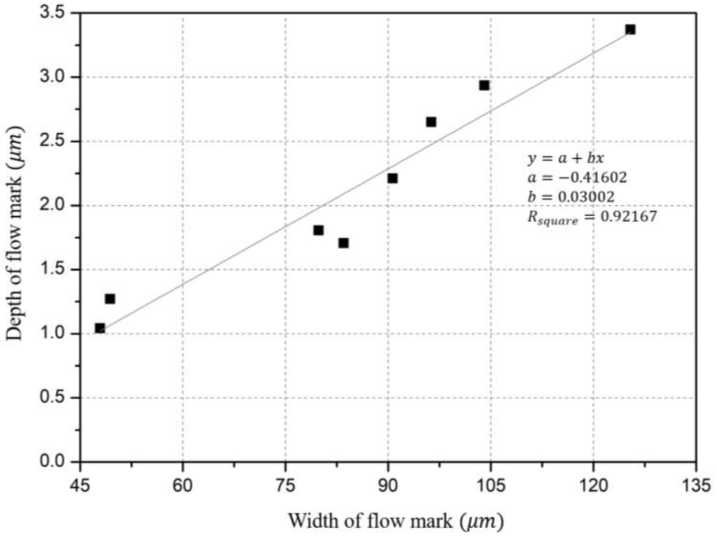

Figure 3.33 The relation between the depth and the width of flow mark (CFD simulation)

Chapter 4

Conclusion

4 Conclusion

In micro-injection molding, there are two major defects which can be occurred in injection stage. One is the defect occurred by cavity filling deviation when the melted resin goes through the runner of mold, and the other is flow mark which is occurred in mold cavity. We investigated the relation between major defects and the major process conditions in micro-injection molding.

For finding the major process conditions which affect to the cavity filling deviation, we did numerical analysis. We investigated the relation between the cavity filling deviation and three process conditions (deviation of runner diameter, wall temperature and gate thickness) with two numerical results: filling fraction and filling time delay. The result of CFD simulation showed that the major process conditions which affect to the cavity filling deviation were the deviation of runner diameter and wall temperature. The mixed condition of those two had the biggest cavity filling deviation.

For reducing cavity filling deviation, we suggested three robust designs: convergent runner model, reservoir model and complex model which is combined with those to models. all models reduced cavity filling deviation effectively, and the complex model had the biggest effect. The reduction of filling fraction was 33% in complex model.

For flow mark which is defect occurred in cavity, we did parametric study in according to “Go-Over” hypothesis. we found three major conditions which affects to the size of flow mark by this parametric study: injection speed, resin temperature and mold temperature. We investigated the relation between the size of flow mark and those three major process conditions by experiment and numerical analysis. The results of both analysis showed that the size of flow mark decreased when injection speed, resin temperature or mold temperature was increased. This result was exactly fitted with the result of parametric study. We also observed the contour of resin flow when the flow mark generated with CFD simulation and it was well fitted with “Go-Over” hypothesis.

References

[1] C A Griffiths, S S Dimov, E B Brousseau and R T Hoyle. 2005. The effect of tool surface quality in micro-injection moulding. *J. Mater. Process Technol*. 189. 1–3. P 418–27.

[2] M Heckele and W K Schomburg. 2004. Review on micro molding of thermoplastic polymers. *J. Micromech. Microeng*. 14. R1.

[3] M F Lacrampe, J Pabiot. 2000. Defects in surface appearance of injection moulded thermoplastic parts – review of some problems in surface gloss distribution. *J. Inject. Molding Technol*. 4. 4. 167–76.

[4] J Giboz, T Copponnex and P Mélé. 2007. Micro injection molding of thermoplastic polymers: a review. *J. Micromech. Microeng*. 17. R96.

[5] B R Whiteside, M T Martyn and P D Coates. 2005. In process monitoring of micro moulding—assessment of process variation. *Int. Polymer Process*. 20. 162–9.

[6] J Zhao, R H Mayes, G Chen, H Xie and P S Chan. 2003. Effects of process parameters on the micro molding process. *Polym. Eng. Sci*. 43. 1542–54.

[7] J Zhao, R H Mayes, G Chen, P S Chan and Z J Xiong. 2003. Polymer micromould

design and micromoulding process. *Plast. Rubber Compos*. 32. 240–7.

[8] L Yu, C G Koh, L J Lee and K W Koelling. 2002. Experimental investigation and numerical simulation of injection molding with micro-features. *Polym. Eng. Sci*. 42. 5. 871–88.

[9] Y Su, J Shah and L Lin. 2004. Implementation and analysis of polymeric microstructure replication by micro injection molding. *J. Micromech. Microeng*. 14. 415.

[10] C Wu and W Liang. 2005. Effect of geometry and injection-molding parameters on weld-line strength. *Polym. Eng. Sci*. 45. 7. 1021–30.

[11] H L Zhang, N S Ong and Y C Lam. 2008. Mold surface roughness effects on cavity filling of polymer melt in micro injection molding. *Int. J. Adv. Manuf. Technol*. 37. 11–12. 1105–12.

[12] M Yoshii, H Kuramoto and K Kato. 1993. Experimental study of transcription of smooth surfaces in injection molding. *Polym. Eng. Sci*. 39. 1251.

[13] T Yashuhara, K Kato, N Otake and T Takaiwa. Seikei Kakou. 1995. (*Proc. JSPP Annual Conf.*) 31.

[14] L Tredoux, I Satoh and Y Kurosaki. 1999. Investigation of wavelike flow marks in injection molding: flow visualization and micro-geometry. *Polym. Eng. Sci.* 39. 2233.

[15] L Tredoux, I Satoh and Y Kurosaki. 2000. Investigation of wavelike flow marks in injection molding: a new hypothesis for the generation mechanism. *Polym. Eng. Sci.* 40. 2161.

[16] H Yokoi, S Nagami, A Kawasaki and Y Murata. 1994. SPE ANTEC 94. 368.

[17] S Y Kang and W I Lee. 2003. Finite element analysis for wavelike flow marks in injection molding. *Master degree thesis. Seoul Nat'l Univ.*

[18] C W Hirt and B D Nichols. 1981. Volume of fluid (VOF) method for the dynamics of free boundaries, *J. Comput. Phys*. 39. 201-25.

[19] C R Swaminathan and V R Voller. 1994. A time-implicit filling algorithm. *Appl. Math. Modeling*. 18. 101-8.

[20] W F Noh and P Woodward. 1976. SLIC (Simple Line Interface Calculation). *The fifth international conference on numerical methods in fluid dynamics.* Lecture notes in phisics. 59. 330-40.

[21] D L Young. 1982. Time-dependent multi-material flow with large fluid distortion. *Numerical methods for fluid dynamics*. 273-85.

[22] N Ashigriz and J Y Poo. 1991. Flux line-segment model for advection and interface reconstruction. *J. Comput. Phys.* 93. 449-68.

[23] G Dhatt, D M Gao and A B Cheikh. 1990. A finite element simulations of metal flow in moulds. *Int. J. Numer. Methods Engrg*. 30. 821-31.

[24] ANSYS FLUENT 15.0 user's guide.

[25] A Cantoni. 1971. Optimal curve fitting with piecewise linear functions. *IEEE Trans. Comput*. C-20. 1. 59-67.

[26] B Hamann and J-L Chen. 1994. Data point selection for piecewise linear curve approximation. *Computer Aided Geometric Design.* 11. 3. 289-301.

[27] J F Agassant, P Avenas, J Pj Sergent and P J Carreau. 1991. Polymer processing: principles and modeling. *Hanser.*

[28] C J Kim. 길잡이 열전달의 기초. 문운당.

국문 초록

미세 사출 성형에서 다중공동금형 내부의 유동 양상 분석

서울대학교 대학원

기계항공공학부

김 범 래

사출 성형 공정은 짧은 공정 시간과 비교적 저렴한 공정 비용으로 인해 가장 널리 이용되는 열가소성 수지 성형 공정 중 하나이다. 특히 근래에 들어서 마이크로 스케일의 제품들을 생산하는데 있어서도 미세 사출 성형이 널리 사용되고 있다. 이러한 미세 사출 성형에서는 제품의 작은 크기 덕분에 생산성을 높이기 위한 방법으로 다중 공동 형태의 금형이 사용되고 있다. 미세 사출 성형의 주입 단계에서 생길 수 있는 몇 가지의 표면 결함들은 광

학 제품 등에 큰 역할을 미칠 수 있으며, 이 결함들과 공정 조건 간의 관계를 규명하여 결함을 최소화하는 것은 미세 사출 성형 공정의 생산성을 높이기 위한 중요한 연구 주제라고 할 수 있다.

미세 사출 성형의 주입 단계에서 생길 수 있는 주요 결함으로는 크게 다중 공동 형태의 특성 상 수지가 러너를 흘러가는 과정에서 생길 수 있는 공동의 충전 편차로 인한 결함과, 공동의 내부에서 생길 수 있는 대표적 결함인 물결 형태의 플로우 마크의 두 가지를 들 수 있다. 본 연구에서는 이 두 가지의 결함과 미세 사출 성형의 주요 공정 조건 간의 관계를 규명하였다.

먼저 주요 공정 조건이 공동의 충전 편차에 미치는 영향을 규명하기 위하여 수치 해석을 실시하였다. 실제 공정을 참고로 하여 러너의 직경 편차, 러너 벽면의 온도 편차, 게이트의 크기 편차 세 가지를 주요 공정 조건으로 정하였으며, 이 조건들이 공동의 충전 편차에 미치는 영향에 대하여 분석하였다. 해석 결과, 공동의 충전 편차에 영향을 미치는 주요 공정 조건은 러너의 직경 편차와 러너의 벽면 온도 편차였으며, 게이트 크기의 편차는 그 영향이 미미한 것으로 나타났다. 특히 러너의 직경과 러너의 온도를 모두 변화시킨 복합 가혹 조건에서 공동의 편차가 가장 크게 나타났다.

공동의 충전 편차를 줄이는 방법으로 세가지의 새로운 형태의 다중 공동 모델을 제시하였다. 수렴 러너 모델, 저수형 모델, 그리고 두 가지 모델을 조합한 복합 모델의 세 가지에 대하여 충전 편차의 저감 효과를 분석하였으며, 세 모델 모두 효과적으로 공동의 충전 편차를 저감시키는 것으로 나타났다. 특히 복합 모델의 경우 순간충전율을 33%까지 저감시키는 결과를 보였다.

수지가 공동 내부를 흐를 때 생기는 대표적인 표면 결함인 플로우 마크에

대하여, 먼저 “Go-Over” 가설을 기초로 한 매개변수 연구를 실시하였다. 그 결과 플로우 마크의 생성과 크기에 대한 관계 식을 얻어내고, 플로우 마크의 생성과 크기에 영향을 미치는 세가지 주요 조건이 주입 속도와 수지의 온도, 공동 벽면의 온도 임을 확인할 수 있었다. 이를 실험과 수치 해석을 통하여 확인하고 플로우 마크의 크기에 대한 최적화를 진행하였다. 그 결과, 실험과 수치 해석 모두 매개변수 연구를 통해 얻은 관계식의 경향성을 잘 따르는 것을 볼 수 있었으며, 플로우 마크의 크기는 주입 속도가 높을 수록, 수지의 온도가 높을 수록, 벽면의 온도가 높을 수록 줄어드는 결과를 보였다. 또한 수치 해석 시 수지 유동 선단의 관찰 결과, “Go-Over” 가설이 실제 플로우 마크의 형성과 잘 맞는 것을 볼 수 있었다.

주요어 : 미세 사출 성형, 다중 공동 금형, 충전 편차, 플로우 마크,
수치 해석, “Go-Over” 가설